Journal of the Meteorological Society of Japan, Vol. 78, No. 4, pp. 301–331, 2000

Gravity-Wave Dynamics of the Hierarchical Structure of Super Cloud Clusters

By Atusi Numaguti[1]

Center for Climate System Research, University of Tokyo, Tokyo, Japan

and

Yoshikazu Hayashi

Geophysical Fluid Dynamics Laboratory/NOAA, Princeton University, Princeton, New Jersey, U.S.A.

(Manuscript received 24 February 1998, in revised form 2 March 2000)

Abstract

The hierarchical structures of eastward-moving tropical super cloud clusters (SCC) and embedded westward-moving quasi-periodic cloud clusters (QPCC) are successfully simulated by a simple longitude-height two-dimensional model with simple moist processes.

The model results clearly show a life cycle of cloud activity. The cloud area starts as a low-level shallow cloud, develops into deep convection, becomes a top-heavy cloud, and decays. Gravity-wave packets are excited by the growth and decay of this cloud and propagate both eastward and westward. The westward-propagating gravity waves are coupled with cloud activity and form westward-moving QPCC. On the other hand, the eastward propagating waves are not immediately coupled with deep convective activity. A deep convective cloud develops only after the low and middle troposphere is sufficiently moistened and cooled. The quasi-periodic emergence of the new convective cloud to the east results in the eastward movement of the envelope of QPCC, forming an eastward-moving SCC.

It is suggested that the excitation of gravity waves of two vertical modes by grow and decay of the heating with top-heavy vertical profile is essential to this hierarchical structure. Especially, the net upward parcel displacement due to the shallow gravity-wave cell have a important role in the generation of new QPCC. Although both eastward-moving SCC and westward-moving SCC are possible in a non-rotating atmosphere with no external origins of east-west asymmetry, eastward-moving SCC can be selected under existence of some external asymmetry, such as the beta effect, mean zonal wind shear, or asymmetry of latent heat flux due to WISHE (wind-induced surface heat exchange) effect.

1. Introduction

The super cloud cluster (or 'supercluster', hereafter referred to as SCC) is one of the most mysterious features of the tropical atmosphere. It is an eastward-moving convectively active region near the equator, with a horizontal scale of 3000–5000 km and a propagation speed of 5 to 10 m/s. SCC was first found in the tropical atmosphere by Nakazawa (1988), and further described by, for example, Lau et al. (1991), Sui and Lau (1992), and Mapes and Houze (1993). Since SCC often appears in the convectively active region of Madden-Julian oscillation (MJO; Madden an Julian 1994), it is considered an inner structure of the MJO. SCC is usually associated with a strong low-level westerly wind, and the intensification of the westerly wind possibly triggers tropical air-sea interaction phenomena such as ENSO (El Niño-Southern Oscillation). Takayabu and Murakami (1991) analyzed the structure of SCC using global objective analysis data and found that the structure has characteristics of a Kelvin-wave.

Another conspicuous character of SCC is its inner structure. Nakazawa (1988) described that there are westward-moving 'cloud clusters' which constitute the low-level structures of the SCC. The horizontal

Corresponding author: Atusi Numaguti, Graduate School of Environmental Earth Science, Hokkaido University, N10W5, Sapporo 060-0810, Japan. E-mail: numa@ees.hokudai.ac.jp

1 Present affiliation: Graduate School of Environmental Earth Science, Hokkaido University, Sapporo, Japan.

scale of these cloud clusters is about 1000 km and the westward speed is about 10–20 m/s. Lau et al. (1991), and Sui and Lau (1992) confirmed this view and stated that westward-moving cloud clusters appears at two- to four-day intervals within a SCC. They further reported that there are also eastward-moving cloud clusters with a similar scale but their occurrence is relatively rare.

Takayabu (1994) found by a spectral analysis of 10-year-period satellite data that westward-moving cloud areas commonly appear in the convectively active region near the equator. The cloud areas have a westward speed of about 20 m/s and appear quasi-periodically at an approximate period of two days. It was concluded that this two-day mode corresponds to the equatorial inertio-gravity wave (Matsuno 1966). The 'cloud clusters' in a SCC seem to correspond to this quasi two-day mode, although the latter appears even outside the SCC. Recent analysis of TOGA-COARE data by Takayabu et al. (1996, hereafter TLS96) revealed the structure associated with the two-day mode, clearly showing that the structure is consistent with the equatorial inertio-gravity wave. With a detailed analysis of TOGA-COARE IOP satellite data, Chen et al. (1996) argued that the convectively active phase of a westward-moving signal consists of several cloud areas, rather than a single cloud area, and that the individual cloud areas do not necessarily move westward even when their envelope moves westward. Hereafter, this westward-moving cloud signal is referred to as 'quasi-periodic cloud clusters (QPCC)'.

The first modeling work relevant to the SCC is that of Hayashi and Sumi (1986), who also introduced the term 'supercluster'. There is, however, no westward-moving substructure corresponding to that of QPCC in their results using a general circulation model. Using numerical models with finer horizontal resolution, Lau et al. (1989) and Itoh (1989) succeeded in simulating the westward propagation of cloud cluster as well as the SCC. In a high-resolution general circulation model experiments of Hayashi et al. (1997), some hierarchical structures of convective activity which resembles the observed SCC-QPCC structure, appear. They showed that strong gravity waves are associated with such convective activities.

Theoretical work concerning the mechanism of SCC is still quite incomplete. The wave-CISK mechanism (Hayashi 1970; Lindzen 1974), which is based on a direct coupling between large-scale waves and cumulus convection through the upward motion of the waves, is one of the candidates for the maintenance mechanism. Numaguti and Hayashi (1991) concluded that the 'SCC' obtained by Hayashi and Sumi (1986), in which the cumulus parameterization of Kuo (1974) is used, is maintained by the wave-CISK mechanism. Recently, the reality of wave-CISK is questioned by several authors (e.g., Emanuel et al. 1995), and the solutions such as obtained by Hayashi and Sumi (1986) are considered to be severely affected by inappropriate cumulus parameterization schemes.

As another mechanism for the maintenance of tropical waves, the WISHE mechanism (Emanuel 1987), or equivalently the evaporation-wind feedback (Neelin et al. 1987), is proposed and found to be potentially important. It assumes that wave-induced modification of surface energy fluxes causes the amplification of waves. Yano et al. (1995, hereafter referred to as Y95) successfully simulated a SCC-like hierarchical structure with a simple, but very-high-resolution shallow-water model. They emphasized the importance of WISHE to the SCC in their model, in which evaporation is large to the east of the convectively active region due to strong easterlies there.

Chao and Lin (1994, hereafter referred to as CL94) also obtained a SCC-like hierarchical structure using a longitude-height two-dimensional primitive equation model. They, on the other hand, proposed a 'cloud cluster teleinduction mechanism' as an explanation for the eastward movement of SCC in their model. They argued that the heating by a cloud cluster generates some circulation, and this circulation excites a new cloud cluster to the east of the existing cloud cluster. However, the dynamical detail of this mechanism was not clarified in their work.

Although the results of these two works (Y95, CL94) show some resemblance to the real SCC, several discrepancies remain. One serious drawback in the result of Y95 (it also appears in Lau et al. (1989), and Itoh (1989)) is existence of an unrealistically continuous cloud area at the eastern edge of SCC. Another problem in common with in Y95 and CL94 is the existence of unrealistically strong easterly wind, in particular, to the east of SCC.

In this study, in order to clarify the dynamics of the hierarchical structure of SCC, a series of numerical experiment is performed by using a simple two-dimensional numerical model. The importance of interaction between clouds and gravity waves of different vertical modes is discussed on the basis of a detailed analysis of the model results. The model and experiments are described in Section 2, while the results of experiments are compared in Section 3. The structures and evolutions of SCC and QPCC are examined in detail in Section 4. The possible mechanism is discussed in Section 5, while summary and conclusion are given in Section 6.

2. The model and experiments

The model used in this study is a simplified version of the CCSR/NIES atmospheric general circulation model (Numaguti 1993). The dynamical framework is based on primitive equations with vertical

coordinate σ, which is the pressure p normalized by the surface pressure p_s ($\sigma = p/p_s$). The prognostic variables are horizontal divergence D, temperature T, specific humidity q, and surface pressure p_s.

The model is applied to the longitude-height two dimensional plane at the equator. Considering that the longitude-height structures of SCC and QPCC can be essentially explained by a Kelvin wave and a westward-propagating inertio-gravity wave, respectively, only the divergence equation is used and the vorticity is set to zero. For a further approximation, the longitudinal scale of circulation is assumed smaller than the meridional scale and all terms that involve meridional differentiations are neglected. However, the beta term, which comes from the meridional gradient of Coriolis factor, is retained. This approximation is the opposite of the longwave approximation (Gill 1980) and should be called 'shortwave approximation'. The validity of this approximation is discussed in the Appendix. The equations are the divergence equation,

$$\frac{\partial D}{\partial t} + \frac{\partial}{\partial x}(uD) + \frac{\partial}{\partial x}\left(\dot{\sigma}\frac{\partial u}{\partial \sigma}\right) = -\beta u - \frac{\partial^2 \phi}{\partial x^2} - \frac{\partial}{\partial x}\left(RT\frac{\partial \pi}{\partial x}\right), \quad (1)$$

the thermodynamic equation,

$$C_P \frac{dT}{dt} = RT\left(\frac{d\pi}{dt} + \frac{\dot{\sigma}}{\sigma}\right) + Q, \quad (2)$$

the moisture equation,

$$\frac{dq}{dt} = S \quad (3)$$

the equation of continuity,

$$\frac{d\pi}{dt} = -D - \frac{\partial \dot{\sigma}}{\partial \sigma}, \quad (4)$$

and hydrostatic equation,

$$\frac{\partial \phi}{\partial \sigma} = \frac{RT_v}{\sigma}. \quad (5)$$

Here, divergence D is defined as

$$D = \frac{\partial u}{\partial x}, \quad (6)$$

where u is zonal wind, and the Lagrangian derivative is defined as,

$$\frac{d}{dt} = \frac{\partial}{\partial t} + u\frac{\partial}{\partial x} + \dot{\sigma}\frac{\partial}{\partial \sigma},$$

where $\dot{\sigma}$ is vertical velocity in σ coordinate. ϕ is geopotential, T_v virtual temperature, $\pi = \ln p_s$, Q diabatic heating, and S is moisture source.

As shown in the Appendix, two types of linear waves exist in the model dynamics. One is an eastward propagating wave and the other is a westward propagating wave. The former well resembles a Kelvin wave and the latter resembles westward-propagating inertio-gravity wave (Matsuno 1966) in the context of the dispersion relation. This indicates that the east-west asymmetry of the dynamics of leading modes of gravity-type wave is qualitatively captured in the two-dimensional model, with this modeled beta effect under the shortwave approximation. The correspondence in dispersion relation is, however, not good for a very long zonal wavelength (> 6000 km) and the dynamics is significantly distorted in the longwave limit. To overcome this problem, the computational domain is restricted to a 90 degree sector along the equator. In this paper, both the westward and eastward propagating waves are simply referred to as gravity waves.

The model uses the spectral conversion method in horizontal descretization. The zonal wavenumbers are truncated at 168 (the actual number of modes is only 43 due to 1/4 sector geometry). The corresponding horizontal grid spacing is about 0.7 degree (80 km). In vertical, the model has unevenly located 11 σ levels. The semi-implicit scheme is used for the time integration and the typical time step is 20 minutes.[1]

The physical processes used in the model are very simple. For the cloud process, only so-called large-scale condensation (LSC) scheme is used. In this scheme the relative humidity in the grid box is adjusted to the saturated value (100 %) whenever it exceeds the saturated value. The condensed water is assumed to precipitate immediately without evaporation. In one experiment, the moist convective adjustment (MCA) scheme (Manabe et al. 1965) is used simultaneously with the LSC scheme. In the MCA scheme, the stratification is adjusted to the moist adiabatic profile with 100 % relative humidity whenever the predicted stratification becomes moist unstable and oversaturated in more than two contiguous model levels. Note that the 'clouds' in the present model with O (100 km) grid size does not correspond to the individual clouds in the real atmosphere, which have the horizontal scale of $\leq$ 10 km. Instead, they are assumed to crudely represent groups of clouds, cloud clusters or 'mesoscale cloud system (MCS)', in O (100) km scale. Also, the cloud activity is not distinguished from the precipitation activity because the model assumes instant precipitation of condensed water.

The vertical eddy transport is implemented by a simple diffusion with a σ-dependent fixed diffusion coefficient. The value is largest at the lowest level (4 m^2/s) and decrease upward linearly in σ. The dry convective adjustment scheme is also applied. The exchange of momentum, heat, and moisture be-

1 Use of the semi-implicit scheme and a relatively long time step may distort the phase speed of gravity waves. It is confirmed, however, that the results are qualitatively the same when a shorter time step is used.

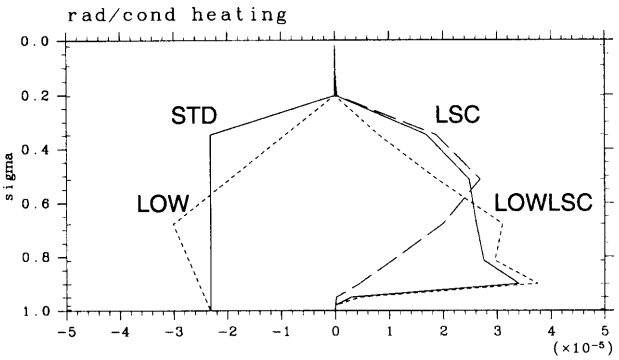

Fig. 1. Heating profiles in the experiments. The left two curves indicate the profiles of prescribed radiative heating. The solid line is for experiments LSC, MCA, NO-BETA, and WISHE, while the dotted line is for experiment LOWLSC. The right three curves indicate the profiles of the simulated condensational heating. The solid line is averaged profile for experiment LSC, while the dotted line is for experiment LOWLSC. The dashed line indicates the composite profile during intense cloud ac- tivity for experiment LSC, which is used in the linear response experiment in Section 5c.

Table 1. List of the experiments.

	β	MCA	radiation	WISHE	SHEAR
LSC	yes	–	STD	–	–
MCA	yes	yes	STD	–	–
LOWLSC	yes	–	LOW	–	–
NOBETA	–	–	STD	–	–
WISHE	–	–	STD	yes(−8 m/s)	–
SHEAR	–	–	STD	–	yes(−5 ∼0m/s)

tween the surface and the atmosphere is estimated by a bulk formula with a constant bulk transfer coefficient, $C_D|v|$. The value, $C_D|v| = 0.0076$, is calculated assuming the roughness, $z_0 = 0.1$ mm, and the observed typical value of wind speed, $|v| = 8$ m/s. Note that the WISHE mechanism is completely excluded by use of the fixed value for $C_D|v|$. The surface is assumed to be completely wet and the temperature is fixed at 300 K. In order to limit the zonal-mean zonal wind speed to a small value, a damping term which restores the zonal-mean component of the zonal wind to zero in 5-day e-folding time is incorporated. These settings are intended to mimic the conditions over the warm water pool in the western equatorial Pacific, where SCC appears frequently. Finally, the radiative process is simply expressed by imposing a fixed cooling rate which is a function of σ only. The standard (STD) profile, shown by the left solid line in Fig. 1 has a constant cooling rate (2 K/day) over most of the troposphere.

The experiments and its settings are listed in Table 1. Experiment LSC is the standard experiment, which uses the LSC scheme as the only condensation process. Experiment MCA uses the moist convective adjustment (MCA) scheme simultaneously with the LSC scheme. Experiment LOWLSC is identical to LSC except that a modified radiative cooling profile is used. The profile is shown in dotted line in Fig. 1, which has a low-level maximum of cooling. In experiment NOBETA, the modeled beta term (βu) in the divergence equation is removed. In this experiment, there is no external origin of east-west asymmetry. The modeled beta term is also removed in experiment WISHE and SHEAR. In the experiment WISHE, the condition of constant $C_D|v|$ is changed only for the surface moisture flux E so that,

$$E = \rho C_D|u + u_0|(q^* - q), \tag{7}$$

where q^* is saturated humidity of surface, u is calculated wind at the lowest level and $u_0 = -8$ m/s. This condition is equivalent to the situation that an 8 m/s easterly mean wind is imposed throughout the atmosphere, allowing the WISHE feedback, and observed from a moving coordinate along with the mean wind. In the experiment SHEAR, on the other hand, a basic wind with linear shear (−5 m/s at $\sigma = 1$ and 0 m/s at $\sigma = 0$) is imposed, and the restoring is applied forward to this sheared basic wind.

At first the model is integrated for about 100 days under the condition of experiment MCA to acquire an equilibrium state. From the final state of this integration, zonally averaged but with small initial random perturbations added, each experiments are integrated for 45 days. Results for the last 30 days are used for the analysis.

3. Results of the experiments

Figure 2 shows the longitude-time distribution of precipitation for each experiment. In the experiment LSC (Fig. 2a), individual cloud areas tend to move westward whereas the envelopes move eastward. The horizontal scale of the cloud area is 100–200 km (a few grids) and that of the envelope is about 2000 km. The westward speed of each cloud area is about 10–12 m/s and the eastward speed of the envelope is about 8 m/s. Each westward-moving cloud area appears about 500 km east of the old cloud area at time intervals of about one day. This behavior is qualitatively very similar to the hierarchical structure of the eastward-moving SCC and the westward-moving QPCC in the real atmosphere, although the lifetime of each cloud area (less than two days) seems a little shorter than the observed QPCC. Thus the westward-moving each cloud area in the model is referred to as QPCC and the eastward-moving envelope as SCC. In some regions, the westward-movement of each cloud area

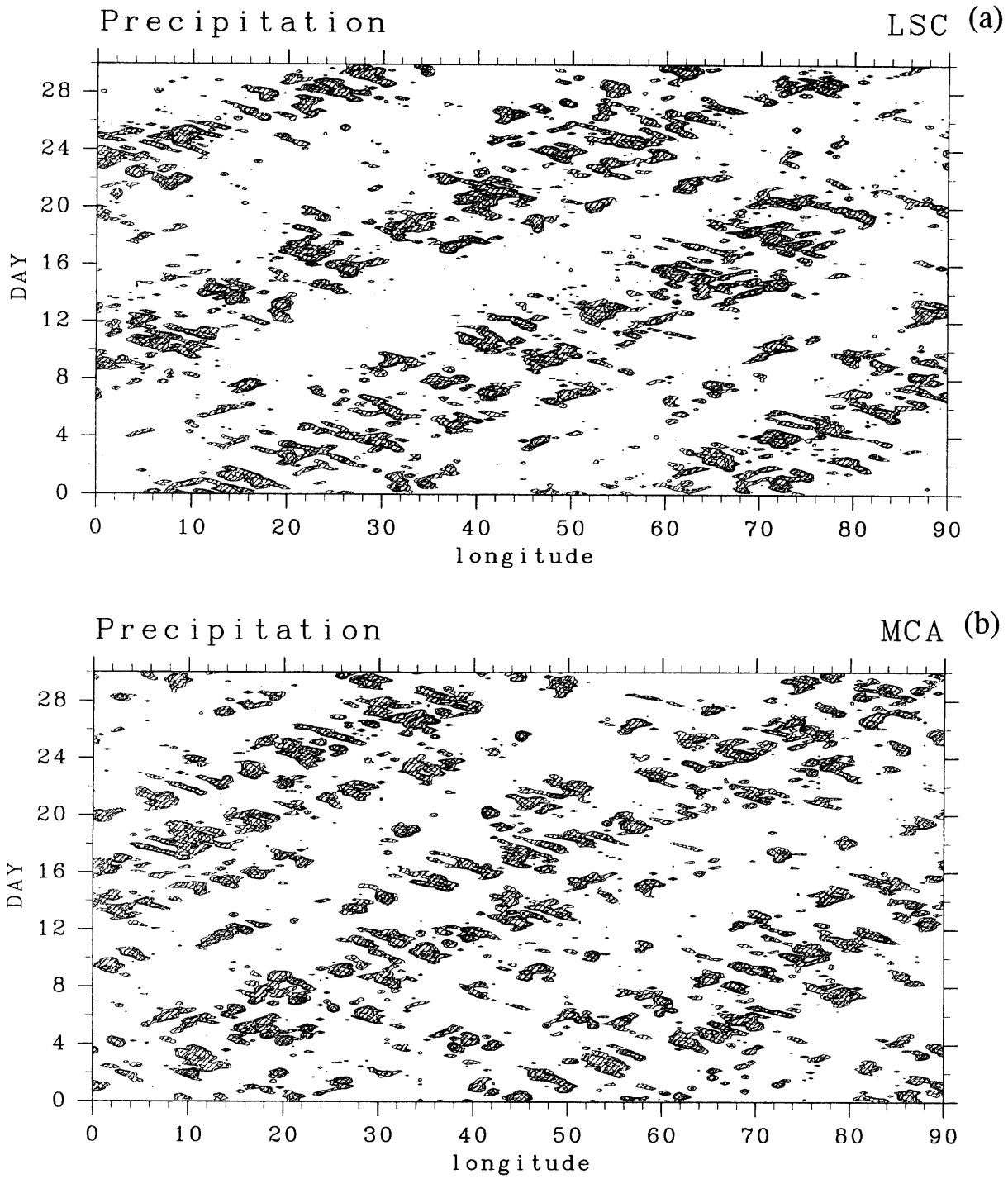

Fig. 2. Longitude-time distributions of precipitation for each experiment. Contour levels are 8, 16, 32, 64, 128 mm/day and the areas over 8 mm/day are shaded. The time axis (days) is directed upward. (a) The standard experiment (LSC), (b) experiment with moist convective adjustment (MCA), (c) with the modified radiative-cooling profile (LOWLSC), (d) without the beta effect (NOBETA), (e) with the WISHE process (WISHE), (f) with basic wind shear (SHEAR).

is somewhat unclear, or there are even eastward-moving cloud areas. However, the westward movement of a group of cloud areas can be traced, for example, from (day 7, 42 degrees) to (day 9, 30 degrees). This behavior seems consistent with the finding of Chen et al. (1996) referred to in the Introduction.

The result of the experiment with the moist convective adjustment (MCA, Fig. 2b), is very similar to that of experiment LSC, showing the promi-

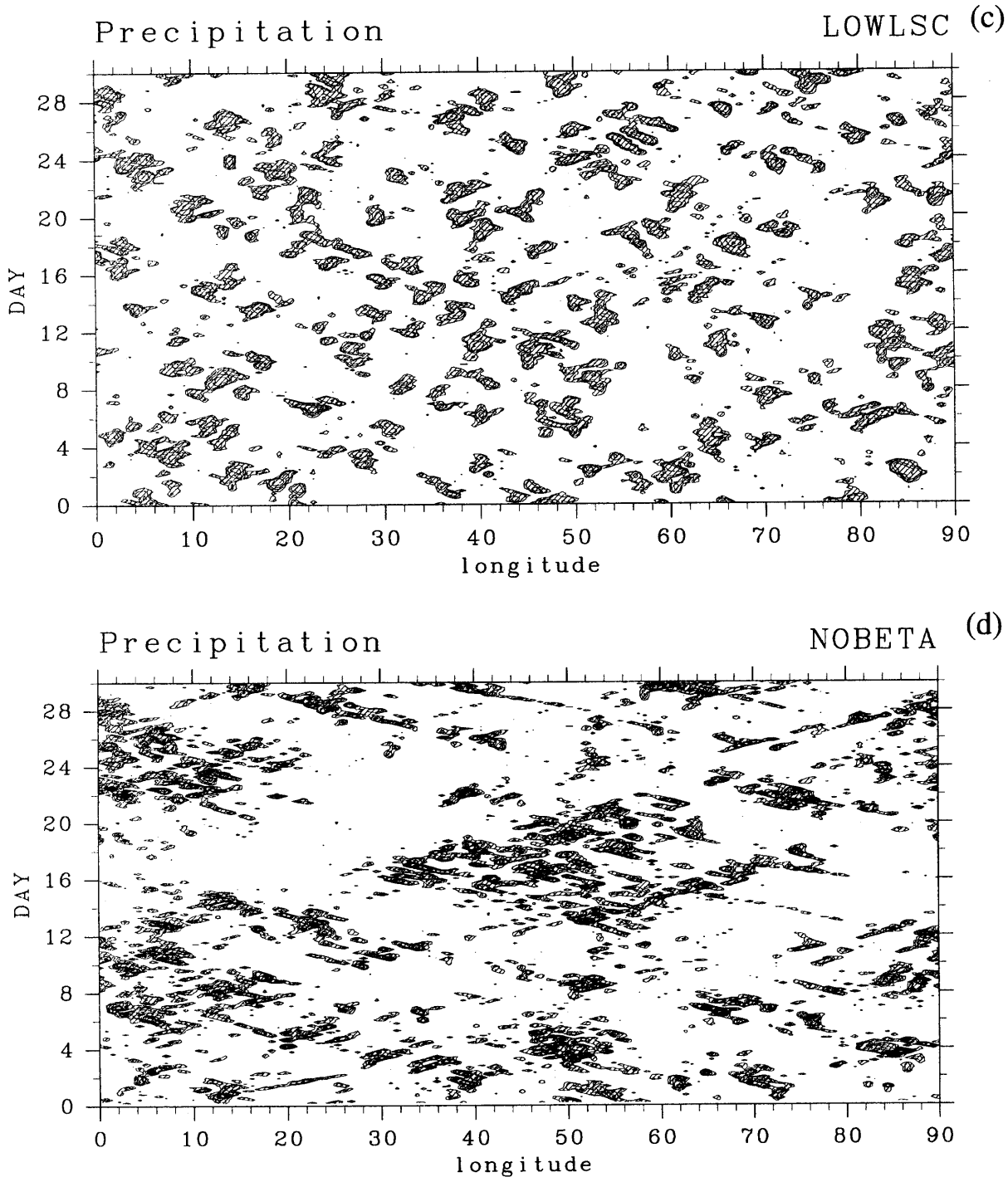

Fig. 2. (Continued)

nent SCC structure. Compared with experiment LSC, however, the lifetime of each cloud area is relatively shorter and the zonal scale of SCC is relatively smaller (about 1500 km). The moist convective adjustment is considered to play only minor role in the formation of the SCC in the model.

When the radiative profile is modified to have a low-level maximum (experiment LOWLSC, Fig. 2c), the result becomes very different. Each cloud area seems to be stationary or move at random, while its lifetime (one to two day) is relatively unchanged. Further, it is difficult to identify SCC-like larger-scale moving envelopes from this figure. The east-west asymmetry, which has clearly appeared in experiments LSC and MCA, is very weak in this experiment.

If the modeled beta effect is removed (NOBETA, Fig. 2d), the result becomes relatively irregular.

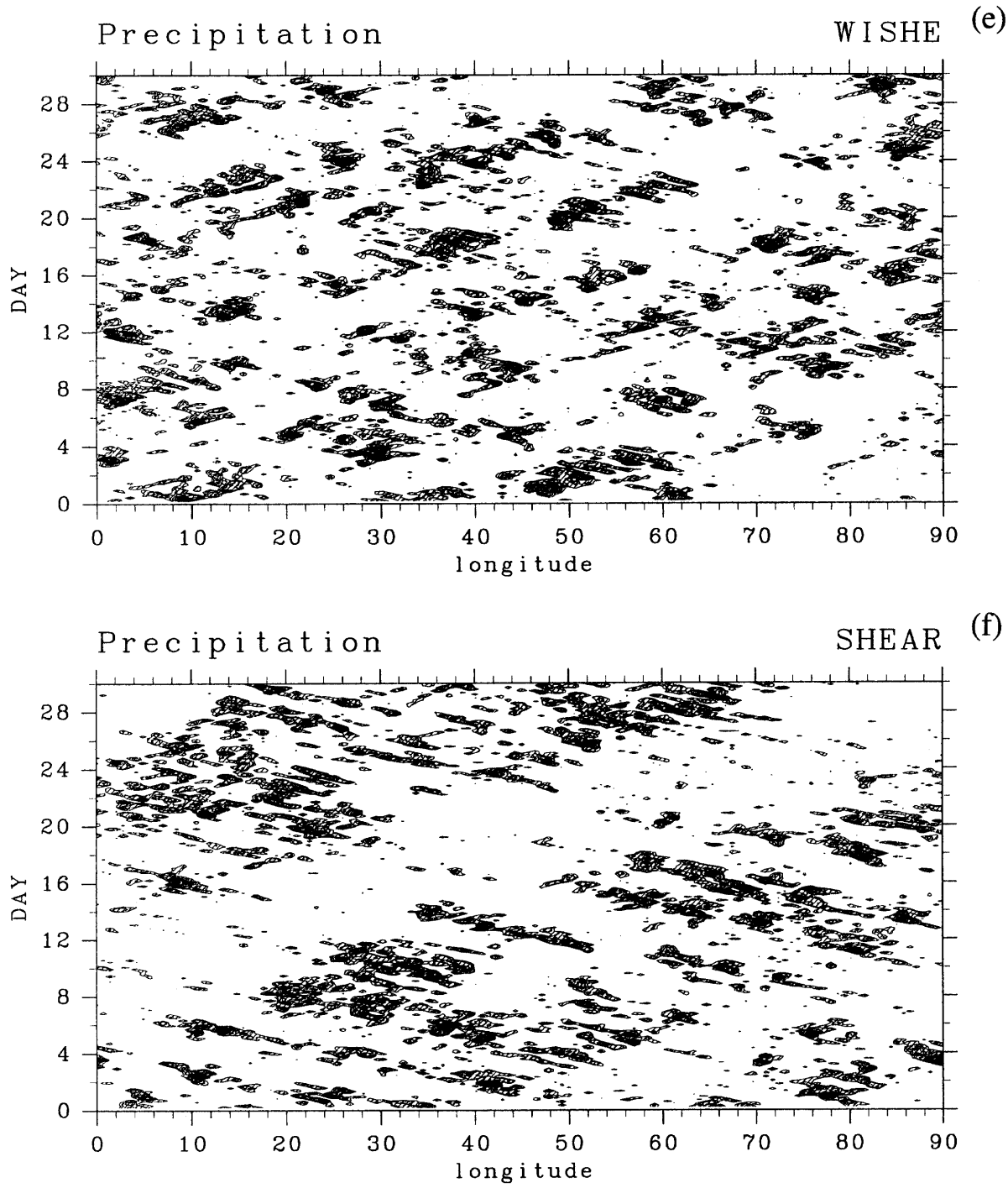

Fig. 2. (Continued)

There are SCC-like structure similar to experiment LSC, for example around (day 8, 10 degrees) and (day 18, 45 degrees). However, we can also recognize *eastward*-moving cloud areas in *westward*-moving envelopes, which should be called westward-moving SCC, for example at around (day 4, 30 degrees) and (day 25, 10 degrees). If we focus on a particular space-time region, the local east-west asymmetry forming SCC, i.e., a moving cloud region with substructure propagating opposite direction, still exists. From a global viewpoint, however, the asymmetry vanishes: Both the eastward- and westward-moving SCCs equally exist. This seems natural because there is no external asymmetry in experiment NOBETA.

Figure 2e is the result of experiment WISHE, in which the WISHE mechanism is allowed with imposed mean easterly (Note that the results are

shown in the moving coordinate along with the imposed mean easterly). Some hierarchical structure is also seen in this experiment, although the east-west asymmetry is relatively weak and individual cloud areas sometimes move eastward. The hierarchical structure also appears in the result of experiment SHEAR, shown in Fig. 2f, in which the mean zonal wind shear is imposed. In experiment SHEAR, the lifetime of QPCCs is relatively longer and westward propagation is clearer compared with other experiments. Note that the speed of this westward propagation (8 m/s) is clearly faster than the mean easterly wind speed (5 to 0 m/s). The results of these two experiments indicate that the east-wast symmetry (coexistence of eastward moving SCC and westward moving SCC) can be broken not only by the modeled beta effect, but also by the WISHE effect or the basic wind shear. When the direction of imposed mean wind is reversed, i.e., when a westerly wind is imposed in WISHE experiment or a mean wind with opposite shear (5 m/s at $\sigma = 1$ and 0 m/s at $\sigma = 0$) is imposed in SHEAR experiment, the results show the anticipated change; dominance of westward moving SCC and eastward moving QPCC.

These results suggest that the radiative cooling profile is important to the formation of the hierarchical SCC-QPCC structure. Another experiment with a strong high-level maximum of radiative cooling (not shown) indicates even a clearer SCC-QPCC structure than LSC. Thus it is considered that the strong cooling in the upper troposphere favors the SCC-QPCC structure. This strong upper-level cooling, however, can also produce the westward-moving SCC as well as eastward-moving one (see, experiment NOBETA, Fig. 2d). In experiments LSC and MCA, the modeled beta effect seems responsible to the asymmetry that the eastward-moving SCC dominates the westward-moving SCC. Such breakdown of symmetry can be also caused by the WISHE effect or the basic wind shear.

4. Structure and evolution of disturbances

This section further analyzes the results of experiment LSC. This experiment is chosen because it has the simplest physics. Although other experiments, MCA, WISHE or SHEAR, might be more realistic, the dynamics may be a little more complicated. The structures and evolution of SCC and QPCC will be described by the use of composite analysis. Three types of composite are examined in the following three subsections. The first is the "QPCC composite", which extracts the structure of westward-moving QPCC, while the second is the "SCC composite" which extracts the structure of eastward-moving SCC. The last is the "life cycle composite", which describes the time evolution of circulations. The reference points for three composites are exemplified in Fig. 3 (The 8 mm/hour contour of precipitation is shown in thick lines. The shadings will be explained in Section 4.3).

4.1 Structure of QPCC

To describe the structures associated with westward-moving QPCC, the reference points for composite are taken from straight lines in the longitude-time plot of precipitation, which approximate the westward movement of QPCC (thick solid lines in Fig. 3). Figure 4 shows composite time-height sections at the reference longitude. The zonal and vertical winds, temperature, and condensational heating are shown in Fig. 4a while the divergence and relative humidity are shown in Fig. 4b. These time-height sections have many features in common with the zonal-height sections (not shown), suggesting simple westward propagation of fixed structure for the first approximation.

Condensational heating starts at low level (between hour -24 to -12), grows upward, and remains only in the upper troposphere higher than the 500 hPa level[2] after hour 6. The upward velocity also shows a similar development: A downdraft appears in the lower troposphere and the updraft becomes confined in the upper troposphere. In the upper troposphere, higher than 600 hPa level, a strong updraft and a warm core exist in the period of intense heating. The peak of the warm signal, however, occurs somewhat earlier than the maximum heating and updraft. This indicates that the circulations have some characteristics of gravity waves. The temperature shows a vertically oscillating signal above 200 hPa. This may be related to gravity waves propagating to the stratosphere, although they are strongly distorted by the insufficient vertical resolution of the model.

In the divergence field (Fig. 4b) there is a large convergence around day 0 at middle (about 700 hPa) levels, rather than at the PBL (planetary boundary layer, approximately lower than 900 hPa). Around hour -8, there is a PBL convergence and upper-level divergence. But after hour -2, a divergence appears in the PBL. Relative humidity is generally high where upward motion exits. The upper troposphere is much more humid after the reference time. In the lower troposphere, a dry signal exists around hour 12, corresponding to the strong downdraft just before.

In simple models of the tropical atmosphere, it is usually assumed that the circulation is dominated by the so-called 'first baroclinic' vertical mode, having one node in the horizontal wind and no node in the

2 Although the figures are plotted in the σ vertical coordinate, the vertical level will be referred to by more familiar pressure values. Each σ surface is very close to the (1000σ) hPa pressure surface.

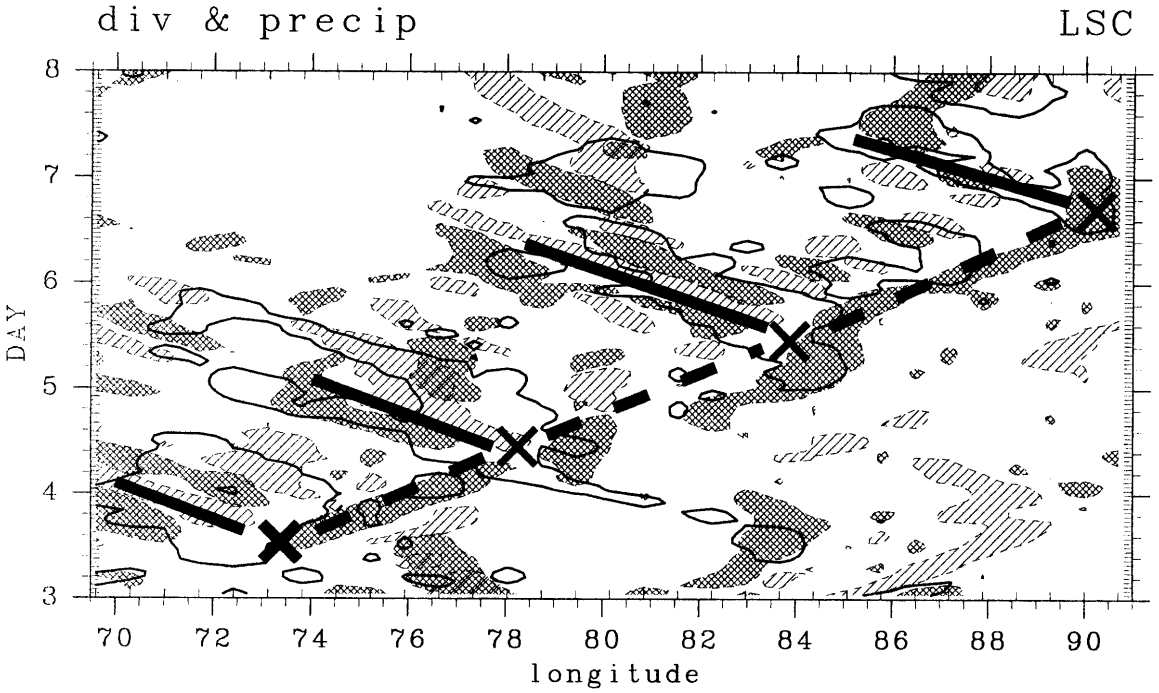

Fig. 3. Longitude-time distributions of precipitation (contours), 900 hPa convergence (dense shading) and 680 hPa convergence (light shading) for experiment LSC. For precipitation, only 8 mm/day contour lines are plotted. Both the dense and light shadings indicate the areas over 5×10^{-5}/s convergence. Reference points for the three type of composite are also shown. The thick solid lines show the reference points for the 'quasi-periodic cloud cluster (QPCC)' composite, the thick dashed lines for the 'super cloud cluster (SCC)' composite, and the crosses for the 'life cycle' composite.

temperature and vertical wind in the troposphere[3] (e.g., Gill 1982). However, the structure of QPCC in Fig. 4 indicates the existence of a shallower vertical structure especially in the later stage of cloud development. The vertical velocity field, which has one node, suggests the importance of the so-called 'second baroclinic' mode. Note that, however, there is a period around hour −4 during which the 'first baroclinic' signal dominates the vertical motion.

TLS96 presented a composite analysis of the 'quasi 2-day wave' (QPCC) by use of radiosonde observations during TOGA COARE IOP. Their Figs. 8–12 and Figs. 15–16 are comparable to the present results (Fig. 4). In general a remarkable similarity is found between their observational results and the present model results. The phase lines tilt from lower to higher altitudes for both the observation and the model results. The intense middle-tropospheric (about 700 hPa) convergence clearly appears in both TLS96's and the present composites. It must be noted that the total depth of cloud and circulations is relatively shallower compared to the observed. This discrepancy may be attributed to the lack of a cumulus parameterization scheme in experiment LSC, and more importantly to the shallowness of prescribed radiative cooling profile (Fig. 1) and the insufficient vertical resolution. It should also be noted that the periodicity of about two days is not so clear in the present model results as the TLS96's observational results. The vertical velocity and humidity signals also have common characters, including the emergence of a downdraft and significant drying in the later stage of cloud activity. For the temperature, consistency between the model results and the observation is good in the low-level signal; a warm signal follows a cold signal. For the upper level signal, however, the amplitude of temperature signal (≥ 1 K) is much larger than the TLS96's result. In the latter, a strong signal exists only in the diurnal variation. Finally, the development of condensational heating in the present results seems consistent with TLS96's results of TBB histogram (their Fig. 6); starting from the lower troposphere, growing up, remaining for a while in the upper tro-

3 Note that the 'first baroclinic mode' here is not the baroclinic mode with largest equivalent depth in the normal mode solution of atmosphere including the stratosphere and upper atmosphere. The 'first baroclinic mode' and 'second baroclinic mode' in this work have equivalent depth of $\sim$ 70 m and $\sim$ 15 m and phase speed of gravity wave of $\sim$ 25 m/s and $\sim$ 12 m/s, respectively. (These equivalent depths and phase speeds are relatively smaller than corresponding values in the real tropical atmosphere, presumably due to lower tropopause height in the model.)

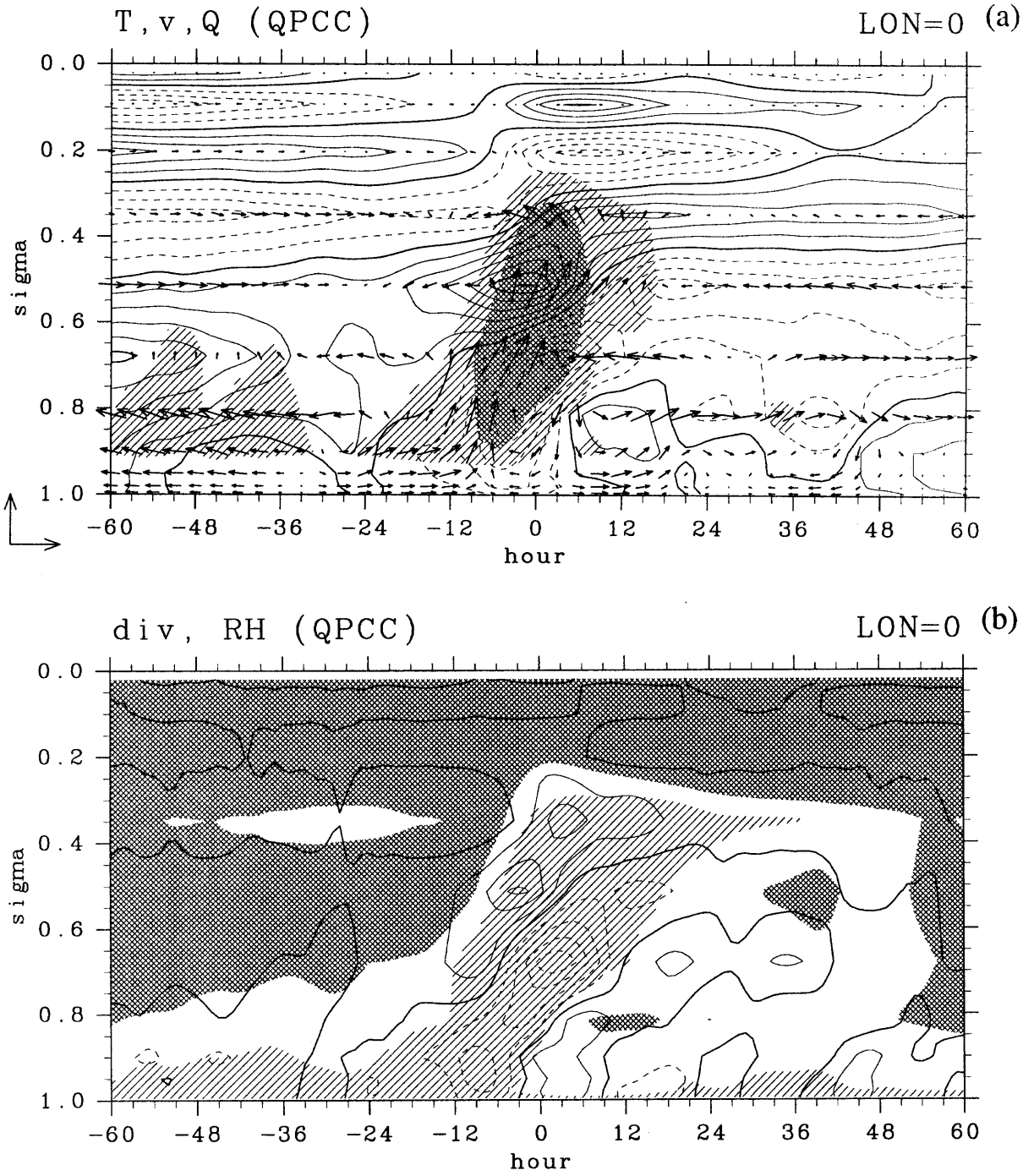

Fig. 4. Structure of QPCC composite for experiment LSC. Time-height (σ) sections at the reference longitude. (a) Temperature (contours, zonal mean substracted), condensational heating (shades) and zonal and vertical σ velocities (vectors). The contour interval is 0.2 K. Light shading indicate grater than 4 K/day, while dense shading indicate grater than 10 K/day. The unit vectors at the lower-left corner represent 8 m/s and 5×10^{-6}/s. (b) Divergence (contours) and relative humidity (shades). Contour interval is 2×10^{-5}/s, light shading indicates the relative humidity higher than 65 % while dense shading indicates lower than 55 %.

posphere, and decaying.

4.2 Structure of SCC

In order to clarify the structure associated with the eastward-moving SCC, the reference points for composite are taken from straight lines in the longitude-time domain, which approximately correspond to the eastward borders of SCC (thick dashed line in Fig. 3). Figure 5 shows the results in a zonal-

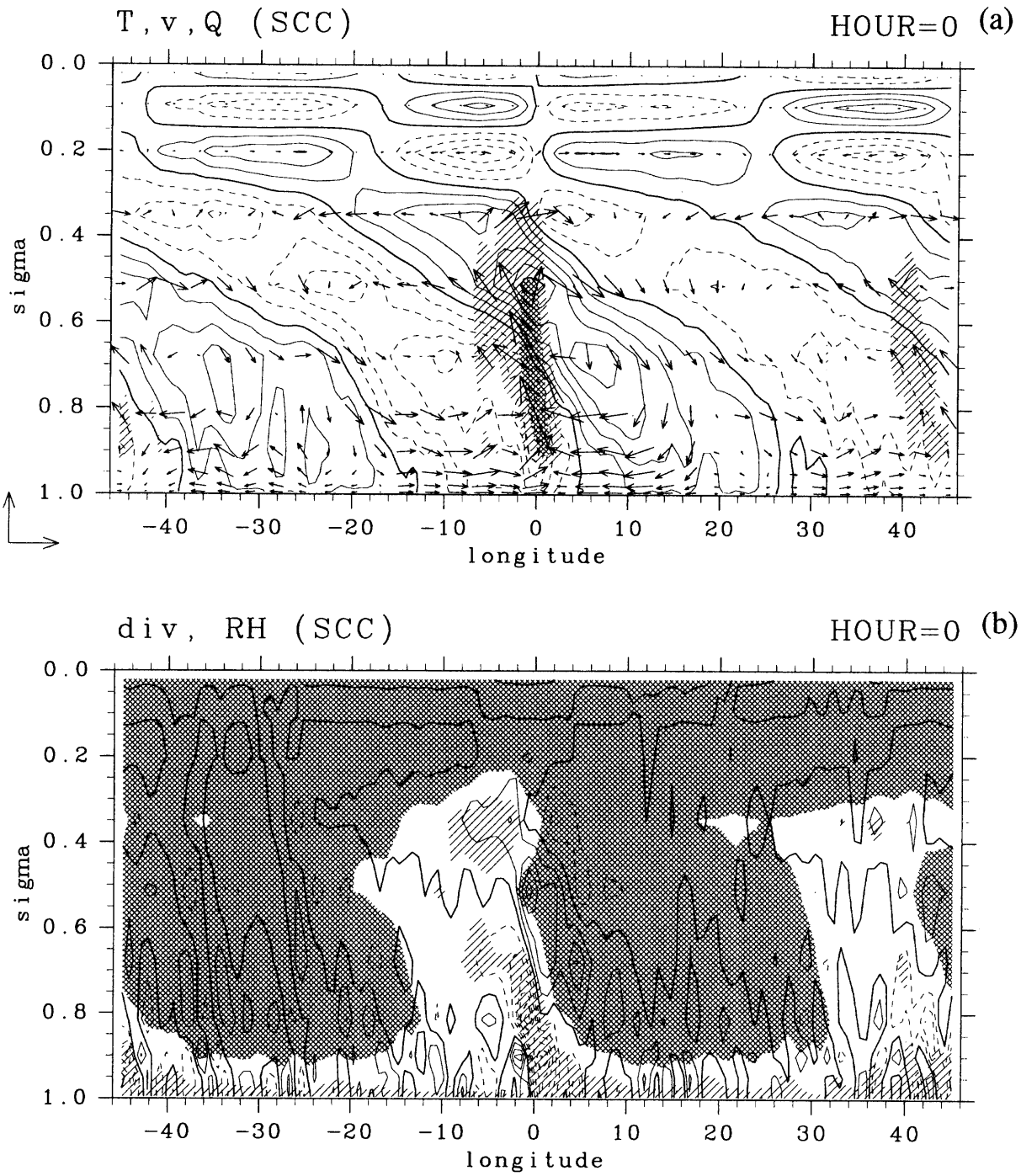

Fig. 5. Structure of SCC composite for experiment LSC. Longitude-height (σ) section at the reference time. (a) Temperature (contours, zonal mean substructed), conden- sational heating (shades) and zonal and vertical σ velocities (vectors). The contour interval is 0.3 K. Light shading indicate grater than 5 K/day, while dense shading indicate grater than 10 K/day. The unit vectors at the lower-left corner represent 6 m/s and 3×10^{-6}/s. (b) Divergence (contours) and relative humidity (shades). Contour interval is 1×10^{-5}/s, light shading indicates the relative humidity higher than 65 % while denseshading indicates lower than 55 %.

height section at the reference time. The pattern of the temperature and zonal wind has a strong westward tilt. Since the structure propagates eastward, the vertical phase propagation is upward. This structure can be regarded as a mixture of the first and the second baroclinic mode signals. The phases of the signals of temperature and zonal wind are approximately coincident in the lower troposphere,

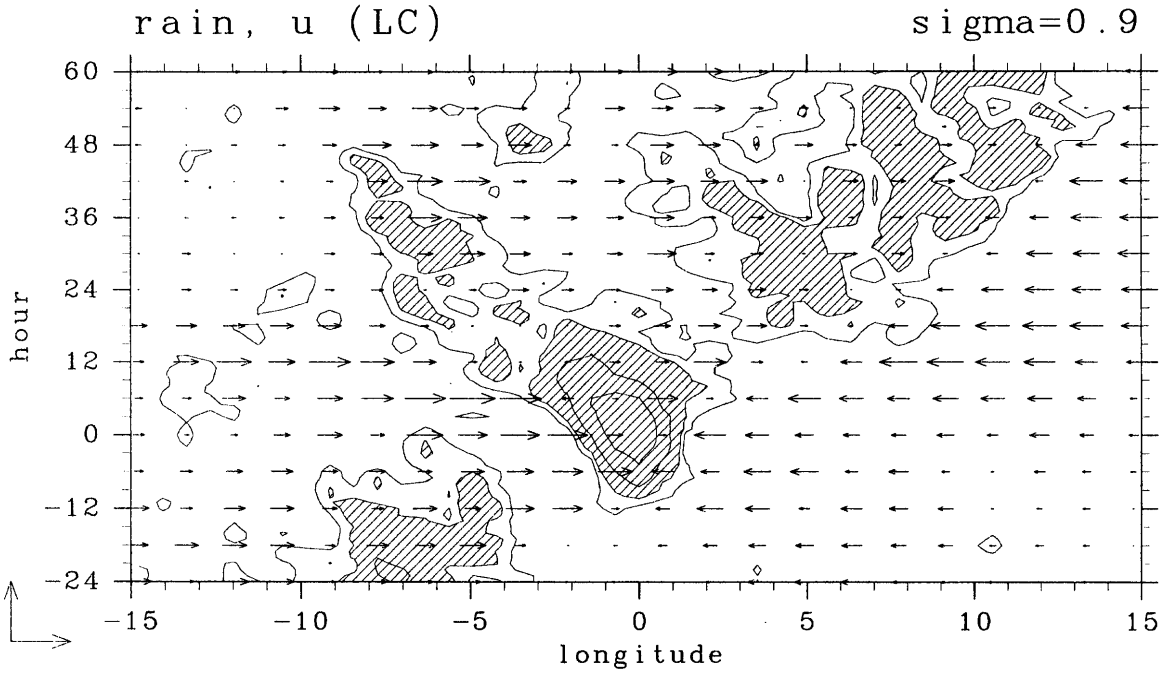

Fig. 6. Longitude-time section of precipitation and zonal wind at $\sigma = 0.90$ of the 'life cycle' composite for experiment LSC. The contour levels are 8, 12, 24, and 48 mm/day with the areas over 12 mm/day being shaded. Unit vector at the lower-left corner indicates 20 m/s. Coordinates are longitude and time relative to the 'radiating event'.

i.e., warm signal is associated with the easterly, and they are almost in quadrature in the upper troposphere. These structure is generally consistent with the observed structure of Kelvin waves. Striking east-west asymmetry exists in the composite of relative humidity (Fig. 5b). In the free troposphere higher than the 900 hPa level, the region to the east of the reference longitude (5 to 20 degrees longitude) is very dry while the region to the west (−15 to 0 degrees) is relatively moist. Near the surface, however, the depth of the wet region (indicated by light shading) is deeper in the region to the east (0 to 20 degrees longitude) than the region to the west (−15 to 0 degrees). This indicates that the relative humidity in the PBL (900–1000 hPa) is generally higher to the east than to the west. The east-west contrasts in specific humidity are similar to these contrast in relative humidity.

The correlation between condensational heating and temperature is an important quantity because it is proportional to the supply of energy into the disturbance through heating. The area of strong condensational heating (indicated in Fig. 5 as dense shading) has a slight westward tilt. The correlation between this part of heating and temperature is small because the temperature perturbation in the lower half of the troposphere is negative. However, there is an additional area of moderate heating in the upper troposphere (light shading) which extends about six degrees to the west of the reference longitude. The positive correlation between the heating and temperature exists owing to this upper-tropospheric moderate heating.

The present structure (Fig. 5) can be compared with the observational results of Takayabu and Murakami (1991), especially with their Fig. 13. The comparison indicates a fairly good correspondence, for example, in westward phase tilt and Kelvin-wave like phase relationship. The main difference is, as in the case of QPCC, that the depth of the entire circulation in the present results is relatively shallower compared to that observed.

4.3 Life cycle of circulations

The above analysis indicates that there are at least two important categories of the vertical structure of the circulations. These are the so-called 'first baroclinic mode' and 'second baroclinic mode' in the troposphere. Corresponding to these, there are two levels of maximum of convergence associated with QPCC, the low level (about 900 hPa), and the middle level (about 680 hPa). The 'first baroclinic mode' has a maximum convergence at low level, while the 'second baroclinic mode' has a maximum convergence at middle level and divergence at low level. In Fig. 3, the low-level (900 hPa) convergence is indicated by dense shading while the middle-level (680 hPa) convergence is indicated by light shading. There are many westward-propagating signals along with the westward movement of QPCC

(thick contours). In addition, there are also distinctive eastward-propagating signals of low-level convergence to the east of each QPCC, almost along the thick dashed line in the figure. Each eastward-propagating signal appears to start from one QPCC and ends at another QPCC. These westward- and eastward-propagating signals appear to be 'radiated' from a common point in the longitude-time domain (exemplified in Fig. 3 as crosses). These points will be referred to as 'radiating events', which are found in almost all QPCCs. By examining in more detail, it is seen that the phase propagation of eastward-propagating low-level convergence is faster than the movement of the system (thick dashed lines). Although the low-level convergence signal almost continuously propagates from west to east, it suspends its propagation and stays at the same position for a while near the radiating event, for example around 84 degrees and 90 degrees longitudes. These combination of fast propagation and stationary period leads to slower eastward propagation of the whole system.

In order to explore the life cycle of the QPCC and its association with the SCC-QPCC structure, the radiating events defined above are used for the reference points for the composite. They are subjectively chosen from the 900 hPa and 680 hPa convergence field. The composite field of precipitation (Fig. 6), plotted with the longitude and time relative to the radiating event, shows a clear sequence of QPCC development. Cloud activity begins about half a day before the reference time, increasing its intensity staying at the same longitude for a while, and start propagating westward at about 10 m/s, and finally decays gradually. The averaged lifetime of QPCC is about two days. Precipitation signals also appear around (hour -24, -10 degrees) and (hour $+24$, $+10$ degrees), corresponding to the QPCC of the previous and next generations, respectively. The signals are, however, diffused and the indication of westward movement is not obvious. This is because the interval of QPCC emergence varies between half a day and two days. On average, a new QPCC appears at intervals of about one day and 6 degrees (700 km). The period is about two days if observed at a fixed longitude (for example, see around -7 degrees longitude) and the zonal 'wavelength' is about 12 degrees (1300 km) if observed at a fixed time (see, around $+24$ hour). Also indicated in the figure by arrows are the composite 900 hPa zonal wind, revealing that westerly winds are strong just around the QPCC. There are also weaker easterly winds to the east. These features seem consistent with the observation.

The longitude-height sections of the composite winds, heating and equivalent potential temperature (θ_e, will be discussed in Section 5.1) for different time references are shown in Fig. 7. Note that the longitudinal range is narrower than Fig. 5. Schematic sequences are given in Fig. 8 to elucidate essential features. At hour -12 (Fig. 7a, Fig. 8a), a low-level cloud area appears around the reference longitude (0 degree). This low-level cloud area is associated with a strong updraft. This updraft constitutes the eastern branch of an anti-clockwise circulation to the west, and the western branch of a clockwise circulation to the east. There is a large cloud area between -4 degrees to -10 degrees longitude. This cloud area is considered a part of QPCC of previous generation (associated with previous 'radiating event'). There is an upward motion, concentrated in the mid- to upper troposphere associated with this western cloud area. It constitutes the western branch of a clockwise circulation with its center around (-3 degrees, 500 hPa). At hour -6 (Fig. 7b), the cloud area around 0 degree longitude is developing into deeper convection. The pair of anti-clockwise and clockwise cells in the lower troposphere intensifies and deepens. The upper western cloud and clockwise cell remain, but the signal have weakened.

At hour 0 (Fig. 7c, Fig. 8b), the cloud area almost extends to the entire tropospheric depth. The previous cloud area to the west has decayed. At hour $+6$ (Fig. 7d, Fig. 8c), the cloud activity near the reference longitude becomes confined to the upper troposphere. This cloud area in general has shifted a little westward from hour 0. The lower potion of the cloud area, however, has split into two areas and shifted to east and west. In this stage, a pair of shallow updrafts appear corresponding to the low-level cloud areas, and a downdraft appears just below the upper tropospheric cloud. They form an anti-clockwise cell centered around (1 deg, 850 hPa) and a clockwise cell centered around (-1.5 deg, 850 hPa). There are also deep circulations, as seen in the downdraft around -8 and $+8$ degrees longitudes, which share the cloudy low-level updraft with the shallow circulations (see, Fig. 8c).

At hour $+12$ (Fig. 7e, Fig. 8d), the upper-level cloud has moved further westward while the updraft of deep convective circulation has decayed. The shallow clockwise cell moved to about -3 degrees longitude while the shallow anti-clockwise cell moved to about $+3$ degrees. Correspondingly, the low-level cloud areas moved with these cells. At this time, however, the eastern cloud area has been disconnected from the main cloud area while the western cloud area is still a part of the main cloud area. Finally at hour $+18$ (Fig. 7f), the center of the upper-level cloud area has moved to about -3 degrees longitude. Around $+6$ degrees longitude, the low-level cloud has intensified along with the updraft there. This situation is very similar to that seen at the hour -12 (Fig. 7a) but the longitude has shifted about 6 degrees eastward.

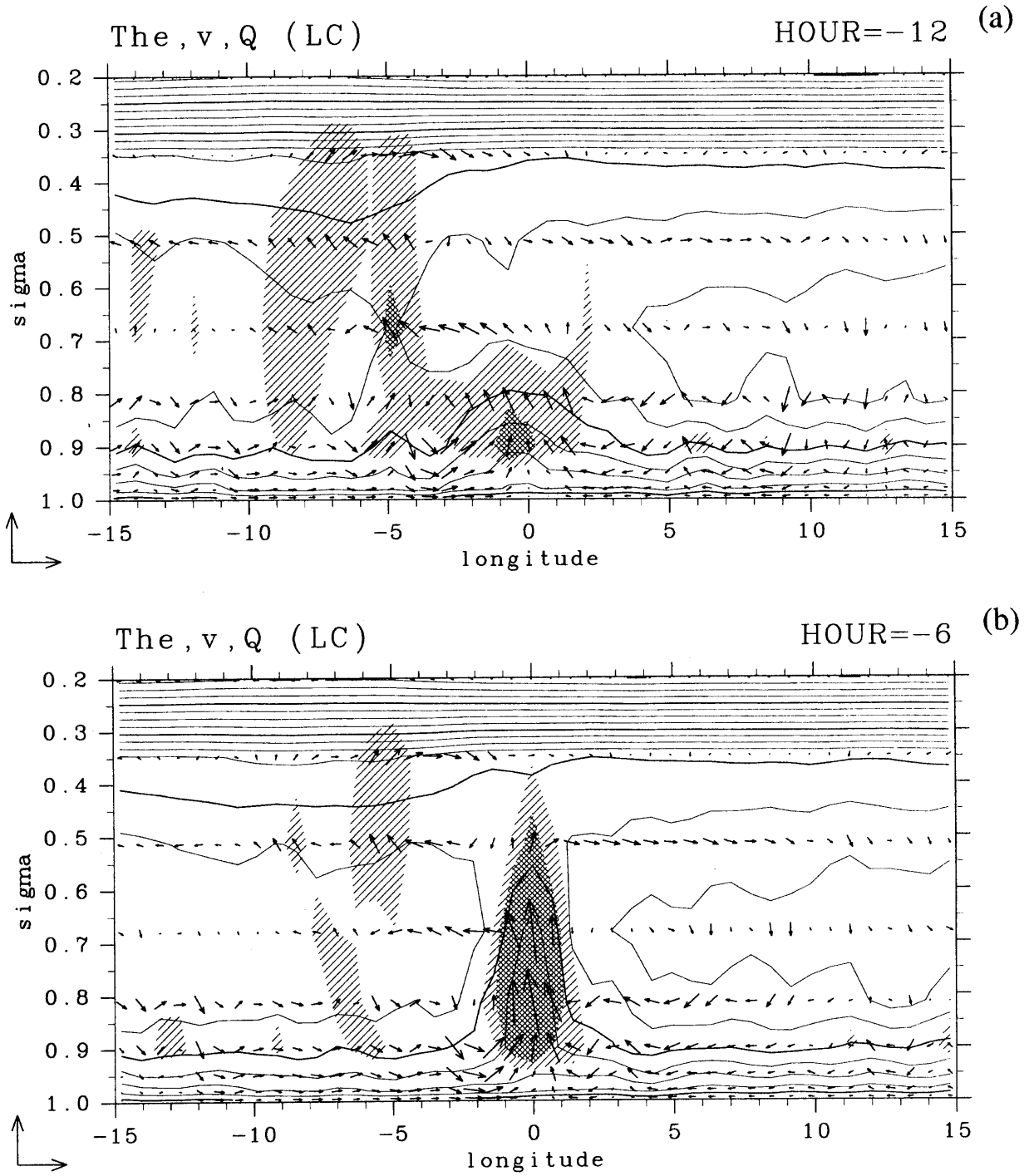

Fig. 7. Structure of the 'life cycle' composite for experiment LSC. Each longitude-height section is at five different times relative to the 'radiating event'. (a) −12 hour, (b) −6 hour, (c) 0 hour, (d) +6 hour, (e) +12 hour, (f) +18 hour. Equivalent potential temperature (contours), condensational heating (shades) and zonal and vertical σ velocity (vectors) are shown. The contour interval is 3 K (thick contour begins 324 K). Light shading indicates greater than 4 K/day. while dense shading indicates greater than 10 K/day. The unit vectors at the lower-left corner represent 15 m/s and 1×10^{-5}/s.

In these composite figures, the existence and movement of the low-level cloud areas during hour 0 to 18 looks continuous. By examining individual cases, however, this is not true. The low-level clouds appear at some times, but disappear at other times. The low-level cloud areas to the west, which are occasionally created with westward-propagating updraft, usually develop into deeper clouds and merge

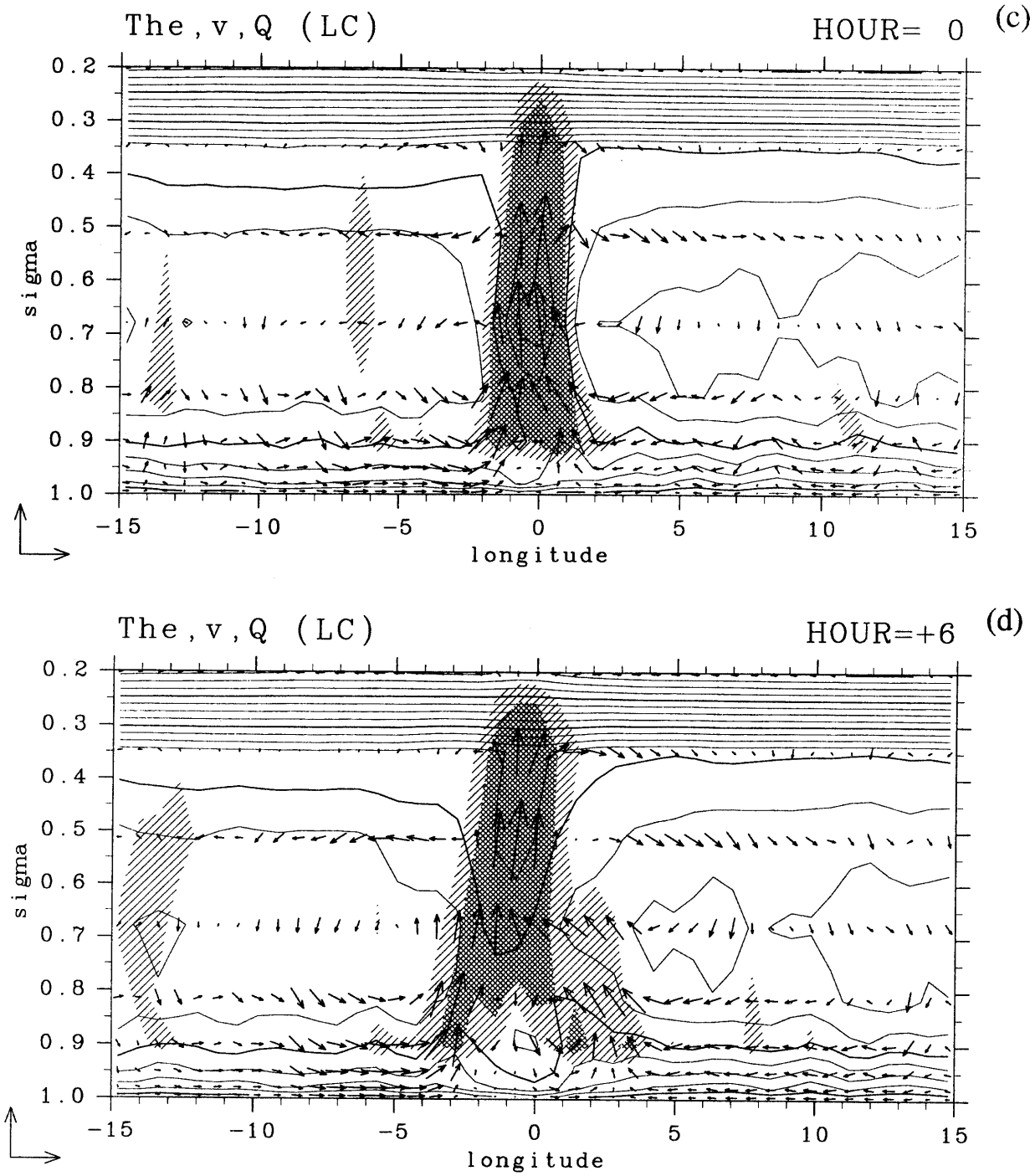

Fig. 7. (Continued)

into the upper-level clouds. On the other hand, the low-level cloud areas to the east, which are also occasionally created, never develop into deeper clouds until hour +18.

Figure 9 represents the longitude-time section of the "life cycle" composite. The value shown is the vertical σ-velocity at low ($\sigma = 0.87$), middle ($\sigma = 0.60$), and upper ($\sigma = 0.43$) levels. Dense shading indicates updrafts, whereas light shading indicates downdrafts. Some features are directly associated with the westward-moving cloud area (thick contours). For example, an updraft signal at $\sigma = 0.60$ occurs almost exactly in the cloud area (Fig. 9b). An intense updraft signal at $\sigma = 0.43$ similarly occurs but with a small time lag (Fig. 9c). However, strong updraft signals and moist signals at $\sigma = 0.87$ (Fig. 9a) are not directly associated with the clouds. It is seen that these signals propagate both eastward

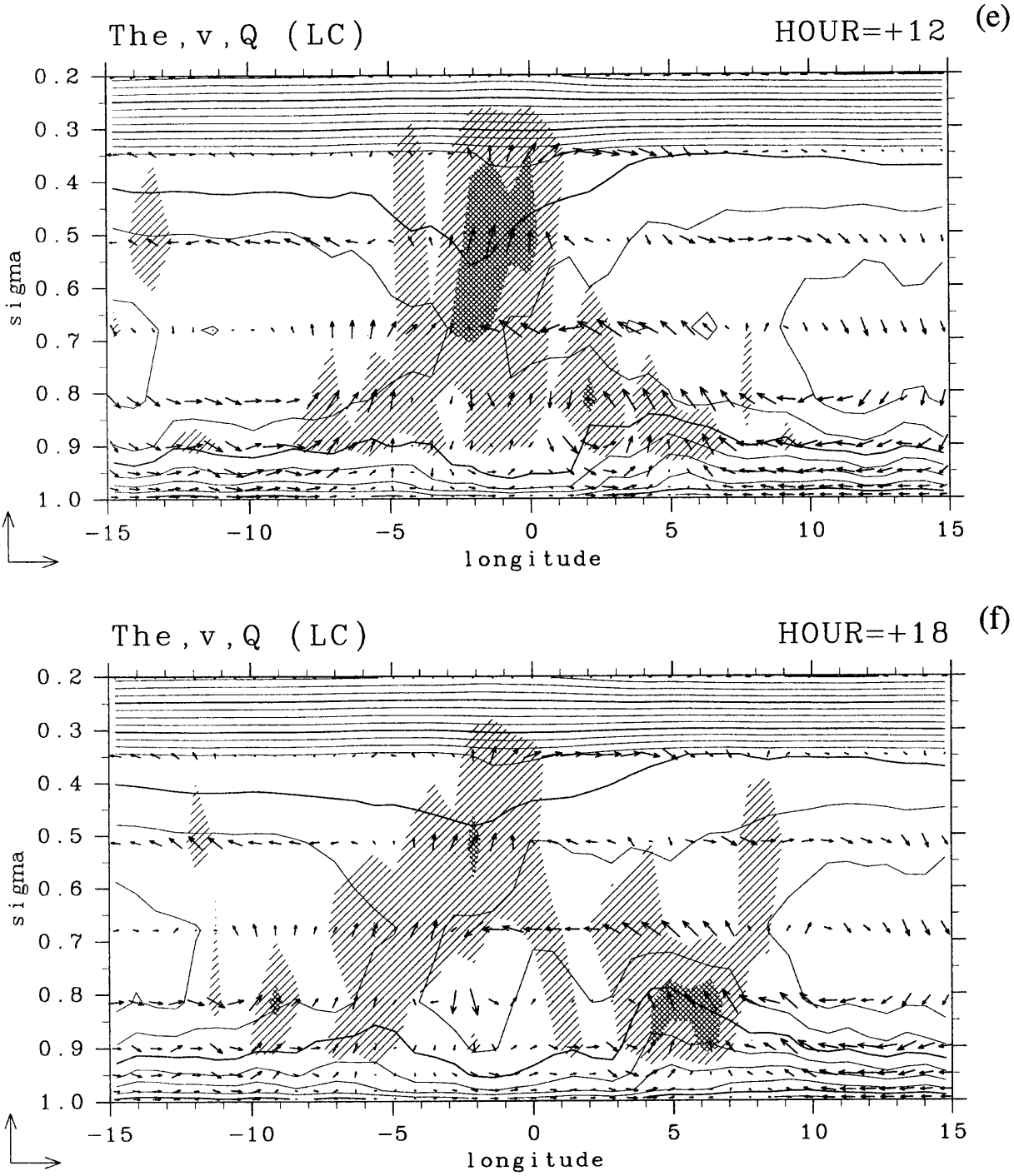

Fig. 7. (Continued)

and westward at approximately constant speed as indicated by straight lines. Some signals appear to start at about (0 degree, hour 0). Other signals start at the same longitude but at about hour 8. This suggests that the 'radiation' of the signal does not occur in a single event but occurs in at least two subsequent events. These signals, which are found even at the middle and upper levels, can be interpreted as propagating gravity waves.

In Fig. 9, there appears at least two dominant waves with different propagation speeds. One propagates 20 degrees in about two days, and the other in about one day, their propagation speeds being about 12 m/s and 25 m/s, respectively. The former signal clearly appears in the vertical velocity field at the lower ($\sigma = 0.87$, Fig. 9a) and the higher ($\sigma = 0.43$, Fig. 9c) levels, with opposite signs between these two levels. The latter signal clearly appears at the

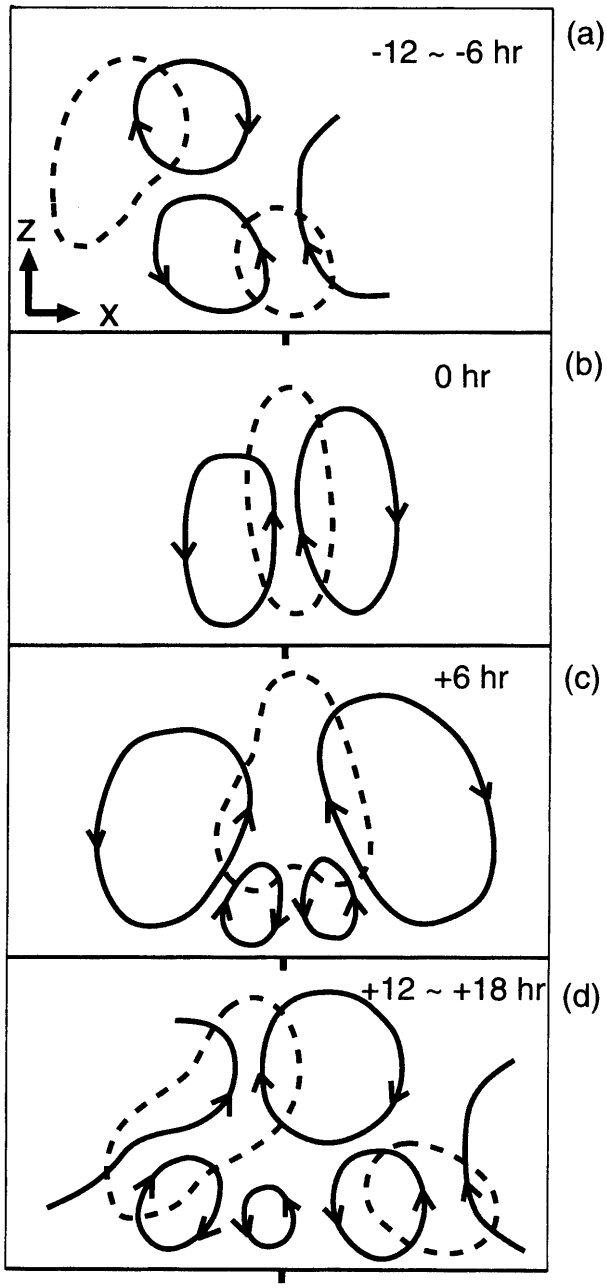

Fig. 8. Schematic illustration of Fig. 7. Circulations (solid curves with arrows) and cloud areas (dotted contours) are shown.

middle ($\sigma = 0.60$, Fig. 9b) level. This faster signals may correspond to the 'first baroclinic' mode in the troposphere, which has a maximum of vertical velocity at middle troposphere. On the other hand, the slower signals may correspond to the 'second-baroclinic' mode, which has maxima of vertical velocity at lower and upper troposphere with opposite sign. Hereafter, the former will be referred to as the 'deep mode' and the latter as the 'shallow mode'. By comparing Fig. 8 and Fig. 9, it is clearly seen that the propagating gravity-wave signal of the shallow mode plays a significant role in the life cycle of QPCC: The westward-movement of QPCC is associated with westward-propagating gravity-wave signals, while the emergence of new QPCC to the east is triggered by eastward-propagating gravity-wave signals.

5. Discussion

In this section, the dynamics of QPCC and SCC is discussed in the context of interaction between clouds and gravity waves. The life cycle of the QPCC can be divided into four stages; (1) the initial development of a stationary convective cloud, (2) the westward movement of circulations with relatively continuous cloud activity, (3) the eastward movement of circulations with cloud activity only at low levels, and (4) the emergence of a new convective cloud to the east. The last stage continues to the first stage of the next generation QPCC. The remaining questions are why the initial convective cloud stationarity grows and decays on about a one-day time scale, how the signals of gravity-wave circulations are excited and propagate, why the westward-moving circulations are associated with clouds whereas the eastward-moving circulations are not, and why the new convective cloud emerges to the east after about a one day period. These questions are examined in the following subsections.

5.1 Development of a stationary convective cloud

To consider the development of a stationary deep convective cloud, the time-evolution of the thermodynamic state and its budget are examined. In Fig. 7, contours show the composite evolution of equivalent potential temperature (θ_e), which is an approximately conserved quantity in the advective and condensational processes. Before the development of a convective cloud (Fig. 7a), the θ_e has a minimum value in the mid-troposphere. During the development of the convective cloud (Fig. 7b and 7c), high θ_e air is advected up to the middle to upper troposphere from the lower troposphere, and the stratification is almost neutralized in the cloud region. After the convective cloud attains the maximum intensity, θ_e in the lower-tropospheric cloud region becomes small (Fig. 7d) and the stratification becomes stable. By this time, the lower-tropospheric cloud activity becomes weak at the reference longitude. Because θ_e is an approximately conserved quantity, this low θ_e air should be advected from some other regions.[4] Figure 7c and 7d suggests that this low θ_e air originates in the middle tropospheric region to the west and east of the convective cloud.

Figure 10 shows the budgets of thermodynamic variables for 680 hPa and 810 hPa level at 0 degree

4 Small peaks in θ_e in the figure are considered due to the nature of composite, which emphasizes signals near the reference longitude.

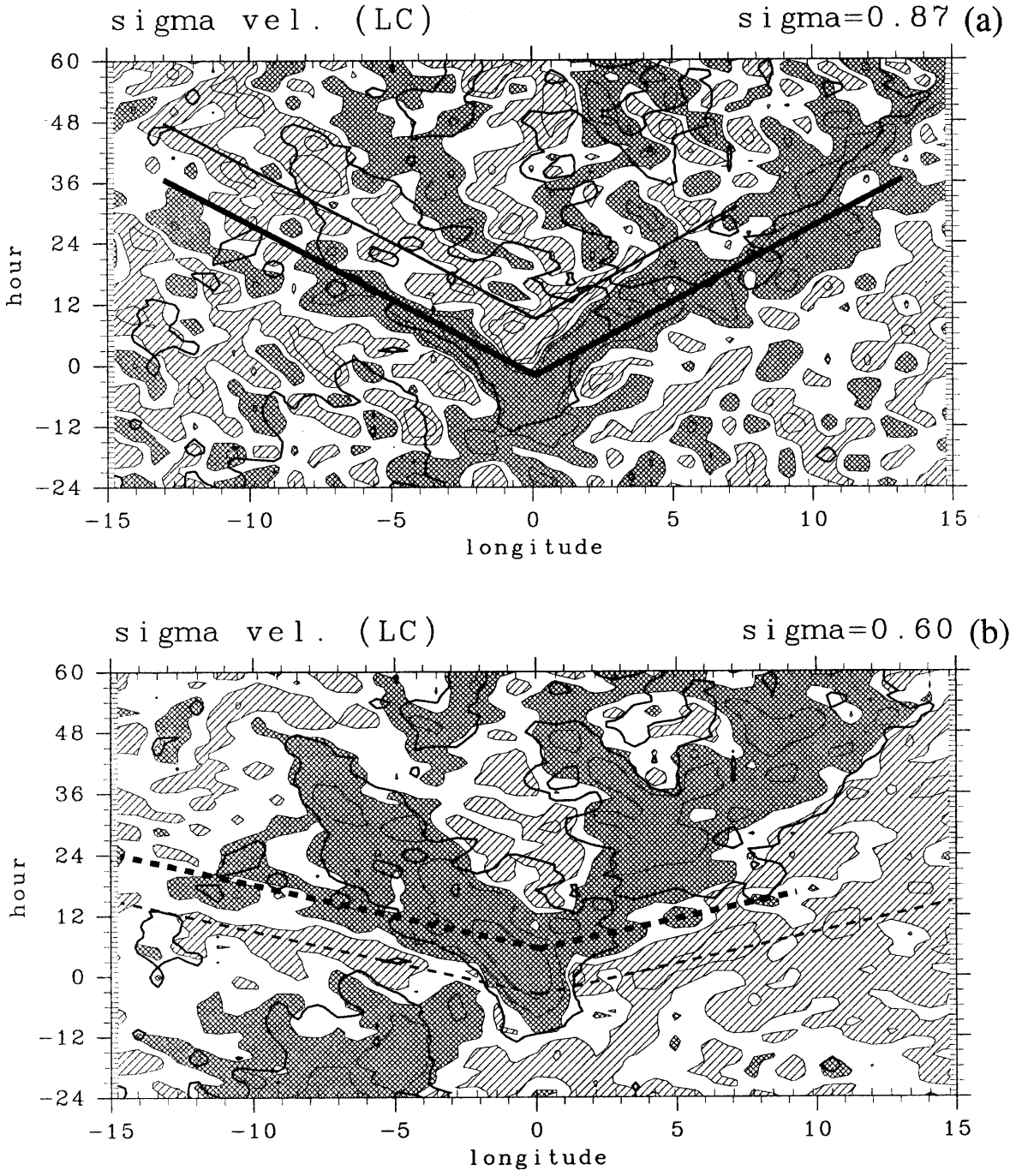

Fig. 9. Longitude-time sections of vertical σ velocity of 'life cycle' composite for experiment LSC. (a) $\sigma = 0.87$ (about 870 hPa), (b) $\sigma = 0.60$ (about 600 hPa), (c) $\sigma = 0.43$ (about 430 hPa). Contour values are -1×10^{-5}, -4×10^{-6}, -1×10^{-6}, $+1\times10^{-6}$, $+4\times10^{-6}$, and $+1\times10^{-5}$/s. Positive values indicate downdrafts. Areas under -1×10^{-6}/s (updraft) are heavily shaded while those over 1×10^{-6}/s (downdraft) are lightly shaded. Thick contours indicate the 8 mm/day contours of precipitation in Fig. 6. Solid and dashed straight lines schematically indicates the propagation of signals (solid: shallow-mode; dashed: deep-mode).

longitude. As shown in the dashed line in (a) and (b), cloud activity (condensational heating; dashed line) begins around hour −10, attains the maximum around hour 0, and starts decaying until it is turned off around hour +10. In the budget of temperature at 680 hPa (Fig. 10a), the adiabatic cooling (dotted line) and the condensational heating are almost balanced and the horizontal advection (dotted-dashed

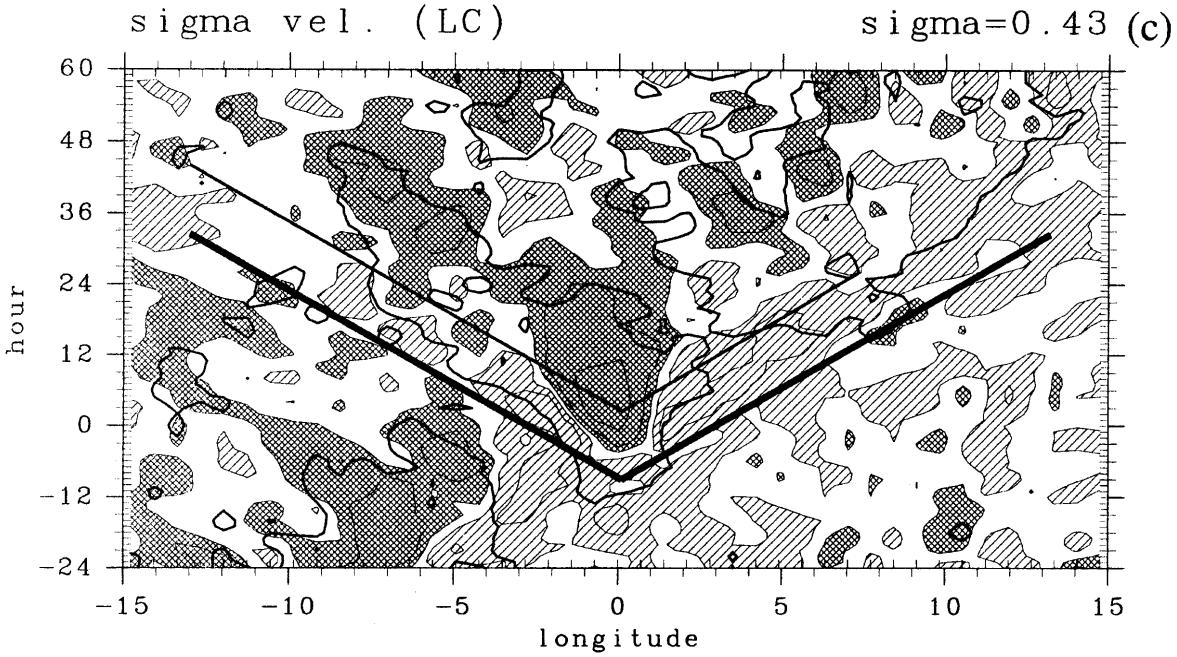

Fig. 9. (Continued)

line) is small. The net tendency is positive near hour −6, suggesting the occurrence of CIFK (conditional instability of the first kind). However, the temperature is cooled down after day 0 during the decaying stage of the cloud activity, indicating the termination of CIFK. When the air is saturated, the temperature and humidity must be closely coupled and determined solely by θ_e, or almost equivalently the moist enthalpy, $C_PT + Lq$. The budget of moist enthalpy (Fig. 10c) is greatly affected by the horizontal advection. After hour 0, a negative tendency due to horizontal advection is significant, resulting in significant net drying and cooling. For this large horizontal advection of moist enthalpy, the advection of moisture Lq has a larger contribution (Fig. 10b) than that of dry enthalpy C_PT (Fig. 10a). At lower level, 810 hPa (Fig. 10d), a similar negative tendency due to horizontal advection is significant at 810 hPa. This negative tendency occurs earlier than that at 680 hPa, and is followed by a further negative tendency by vertical advection due to the downdraft. In Fig. 10c and 10d, sum of the horizontal and vertical advection terms are plotted in thin solid line. The difference between this and the thick solid line (total advection) represents the effects of diffusion and radiation. It can be seen that the effects of diffusion and radiation are not important in the budget near the cloud region, although they are essentially important in the maintenance of zonally mean field.

From these analyses, it is suggested that the CIFK process is responsible for the stationary development of cloud activity and that the horizontal advection of the ambient dry, low θ_e air is responsible for the cooling of the lower troposphere, termination of CIFK, and decay of the cloud activity. From a Lagrangian viewpoint, the effect of horizontal advection should be significant when the displacement becomes comparable to the size of the circulation. This condition can be written as

$$\frac{UT}{L} \simeq \frac{WT}{H} \simeq DT \simeq O(1), \tag{8}$$

where T, U, W, L, H, and D are the representative values of time, horizontal and vertical velocity, width and depth of the circulation, and divergence. Then the time scale should be $T \simeq H/W$, which is a turn-over time of the circulation (or 'direct adjustment time scale', Bretherton 1994). In the present model, $D \sim 3 \times 10^{-5}$ (see Fig. 3) and the time scale $H/W \simeq D$ is about 3×10^4 sec, about half a day. This estimation is consistent with the duration of the deep convective clouds in the model.

5.2 Propagation of gravity-wave signals

It is suggested that propagating gravity-wave signals play a key role in the life cycle of QPCC. The signals appearing in Fig. 9 are schematically summarized in Fig. 11. As seen in Fig. 9, there are 2×2 types of signal in the vertical velocity field; a deep-mode updraft (thick dashed lines in Fig. 11), a deep-mode downdraft (thin dashed lines), a shallow-mode low-level updraft (or upper-level downdraft — thick solid lines), and a shallow-mode low-level downdraft (or upper-level updraft–thin solid lines). Note that

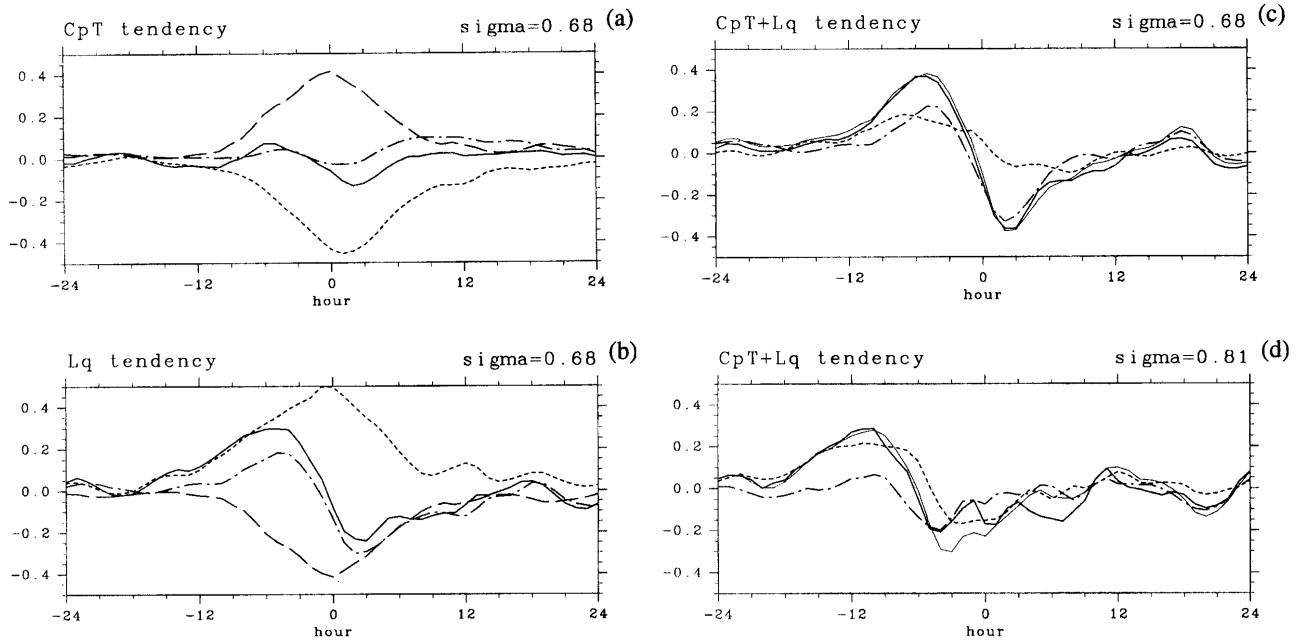

Fig. 10. Time evolution of the individual budget term for temperature C_PT, humidity Lq, and moist enthalpy $C_PT + Lq$ of the 'life cycle' composite for experiment LSC at the reference (0 degree) longitude. Unit is J/kg s^{-1} (0.4 J/kg s^{-1} corresponds 33 K/day). (a) Terms in the heat budget at the $\sigma = 0.68$ level. (b) Terms in the moisture budget at the $\sigma = 0.68$ level. (c) Terms in the moist enthalpy budget at the $\sigma = 0.68$ level. (d) Terms in the moist enthalpy budget at the $\sigma = 0.81$ level. Thick solid line: total tendency, dashed line: condensation term (only in (a),(b)), dotted line: vertical advection (including adiabatic cooling), dotted-dashed line: horizontal advection, thin solid line: total advection (only in (c),(d)).

the lines in Fig. 11 indicate the center (maximum) of the decomposed signals and the actual field (Fig. 9) corresponds to a superposition of signals with a finite width.

For the deep-mode signals (dashed lines — fast propagation), downdraft signals first start propagating from about (0 degree, hour 0), and updraft signals follow, starting around hour 8. For the shallow-mode signals (solid lines — slow propagation), on the other hand, low-level updraft signals first start propagating and low-level downdraft signals follow. As seen in Fig. 7 (see also Fig. 8), pairs of updraft and downdraft signals form closed circulations, or 'gravity-wave cells'. The westward movement of QPCC approximately corresponds to the propagation of the shallow-mode low-level downdraft (or upper-level updraft).

Bretherton and Smolarkiewicz (1989, referred to as BS89) and Nicholls et al. (1991, referred to as NPC91) discussed the formation of gravity waves from a specified heating, which is turned on as a step function in time and has an infinitesimal horizontal width. Spatially concentrated signals of downdraft (wave-heads) are excited when the heating is turned on, propagating in both directions at the speed of free gravity waves, warming the atmosphere behind them. Because the phase speed of gravity wave depends on the vertical wavelength, the wave-heads of different vertical wavelengths will disperse and be separated out from each other as the time advances. By examining the consequences after the heating is turned off some time later, Mapes (1993, referred to as M93) described the generation of gravity-wave cells. The turn-off of heating excites wave-heads which have opposite directions to those excited by the turn-on, and pairs of downdrafts and updrafts excited by turn-on and turn-off form propagating closed cells. For example, downdraft wave-head excited by turn-on and updraft wave-head excited by turn-off of the 'first baroclinic' mode form propagating closed cell having upper- and low-level horizontal flows between two wave-heads. Also, the turn-on and turn-off wave-heads of the 'second baroclinic' mode form two-story closed circulations. The signals in Fig. 11 can be interpreted as these gravity-wave cells although the heating in the present model does not behave as a step function as in BS89 and M93. As easily derived from the solution of BS89, the response of vertical velocity w is proportional to the time-derivative of the heating;

$$w \propto -\frac{1}{C}\frac{\partial \hat{Q}}{\partial t}\bigg|_{t-\frac{|x|}{C}} \tag{9}$$

when the heating $Q(x,t)$ has an infinitesimal spatial width, $Q(x,t) = \hat{Q}(t)\delta(x)$.

The response will then be dominated by the gravity-wave heads from the maximum growth and

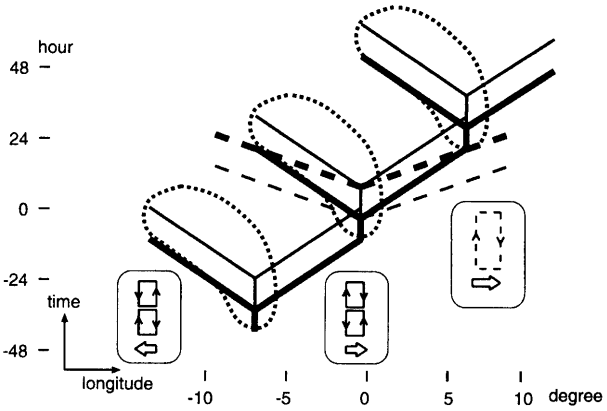

Fig. 11. A schematic representation of vertical velocity signals appearing in Fig. 9 in a longitude-time domain. Solid lines indicate the propagation of the shallow-mode components of signals while the dashed lines indicate the deep-mode components of signals. Thick lines indicate low-level updraft and thin lines indicate low-level down- draft. The upper-level vertical velocity is the same (opposite) direction to the low- level vertical velocity for deep(shallow)-mode components. The non-propagating convective updraft in the early stage of the life cycle is indicated by a short vertical line around (0 degree, hour 0). Some signals are omitted for brevity. Cloud areas are shown in dotted contours. Schematic form of the circulations in longitude-height domain are also shown.

maximum decay of the heating. The former corresponds to the signals starting around hour 0 and the latter corresponds to those starting around hour 8. Although the heating in the present model has a finite width, the qualitative behavior of response may not be much different from the infinitesimal-width case, provided that the width is relatively small (NPC91). One significant difference from M93 is, however, the existence of the remaining westward-moving heat source and many westward-propagating signals associated with it.

5.3 Importance of the heating profile

Examining the behavior of gravity wave signals excited by turn-on of heating followed by its turn-off, M93 pointed out that a net upward displacement of low-level air parcels from initial state appears at remote location a little distant from the heating. M93 suggested that this upward displacement will increase low-level humidity and trigger the next convective clouds near the original cloud. He also pointed out that the parcel displacement by wave-head signals is sensitive to the vertical profile of heating, and that this 'gregarious convection' effect is active only with a top-heavy heating profile, i.e., the upper-tropospheric heating is stronger than the lower-tropospheric heating. If the heating has a top-heavy profile, the switch-on heating excites not only a pair of downward wave-heads of 'first baroclinic mode' (deep mode) but also a pair of 'second baroclinic mode' (shallow mode) wave-head, which have downward motion in the upper troposphere and upward motion in the lower troposphere. This is due to the top-heavy heating profile can be decomposed into a positive 'first baroclinic' heating with maximum at middle level, and a 'second baroclinic' heating with positive (negative) heating in the upper (lower) troposphere.

Observing at a fixed location, the parcel displacement from the initial state becomes negative after the passage of a deep-mode wave-head excited by the turn-on. Then owing to the passage of updraft wave-head excited by the heating turn-off, the parcel displacement returns to the initial level. If we consider the effects of deep-mode wave only, the parcel displacement from initial never reaches a positive value. If we consider the effects of sallow mode, on the other hand, the first signal excited by turn-on is a wave-head with low-level updraft, and the second signal excited by turn-off is a wave-head with low-level downdraft. Then the low-level parcel displacement between the passage of these two shallow-mode wave-heads becomes upward. These effects on parcel displacement of wave-heads of deep and shallow modes are competitive. The low-level parcel displacement becomes positive only after the downward displacement by the deep-mode downdraft was canceled by the deep-mode updraft due to turn-off, and after the shallow-mode updraft due to turn-on has been passed through, but before the shallow-mode downdraft due to turn-off arrives. Such a condition can be fulfilled at a remote location distant from the heating, since the propagation of the shallow-mode signal is slower than that of deep-mode signal (see, Fig. 11).

With a bottom-heavy heating case, however, the low-level net displacement never becomes positive because even for the shallow-mode, the downdraft excited by turn-on comes first and the updraft excited by turn off follows it. The occasional existence of low-level clouds behind the propagating low-level updraft, as seen in Fig. 7 (Section 4), and the emergence of a new convective cloud to the east are considered consistent with this gregarious convection effect by the top-heavy heating.

In order to demonstrate this effect, responses to a prescribed heating is calculated using the same model but with all physical processes removed. An approximately linear response is derived by imposing a small-amplitude heating. The time- and zonal-mean state of experiment LSC, with the zonal wind set to zero, is used for the initial state of the calculation. The vertical profile of heating is assumed

constant and derived from the composite profile averaged between hour 0 and hour 8 at the reference longitude (Fig. 7). The profile, which has top-heavy characteristics, is shown in Fig. 1 as dashed lines. The time evolution of the heating is assumed to take sinusoidal form:

$$Q(x,t,\sigma) = \begin{cases} Q_0(\sigma)X(x)\cos(\pi t/T), & \text{for } |t| < T/2 \\ 0, & \text{otherwise} \end{cases} \quad (10)$$

where the duration of the heating T is specified as 12 hours. The horizontal shape $X(x)$ also takes sinusoidal form with a peak at the 0 degree longitude, and non-zero values of the heating exist at five grid points ranging ± 2 degrees.

The results for σ-velocity (positive downward), and specific humidity, which is proportional to the upward displacement, at the lower level ($\sigma = 0.90$) are shown in Fig. 12a and 12b, respectively. In Fig. 12a, a weak downward signal (around hour 4 at 5 degrees), which corresponds to the deep-mode signal, appears at first. It is followed by a strong upward signal, which is a mixture of the deep-mode and the shallow-mode signals. Then a strong downward signal follows further, which mainly corresponds to the shallow-mode signal but mixed with signals of higher vertical modes. These behaviors are generally consistent with the results of the full-model shown in Fig. 9. Corresponding to these signals in vertical velocity, a weak dry signal appears first and a strong moist signal follows in the humidity field (Fig. 12b). After these signals, there are minor dry and moist signals having a slower propagation due to higher vertical modes. At the longitude of heating (0 degree), the humidity decreases as soon as the heating weakens.

Figure 12c shows the response for a different, bottom-heavy (maximum at lower troposphere) heating profile, which is similar to the dotted line in Fig. 1. The response is very different from that with top-heavy heating (Fig. 12b). A large decrease of humidity (downward displacement) occurs when and where a large increase occurs in the top-heavy heating case. An increase of humidity remains at the longitude of heating, also contrary to the top-heavy case. Only a weak increase of humidity occurs around (hour 24, $\pm$ 3 degrees) by the effect of slowly-propagating higher vertical modes. These results also indicate that the top-heavy heating is important to the existence of the shallow-mode gravity-wave cells with an upward displacement.

Figure 1 compares the heating profiles for two experiments; LSC (solid lines) and LOWLSC (dotted lines). The positive condensational heating (right) almost balances the negative radiative cooling (left) except in the lower troposphere and the condensational heating in the upper troposphere is significantly stronger for LSC than that for LOWLSC. It

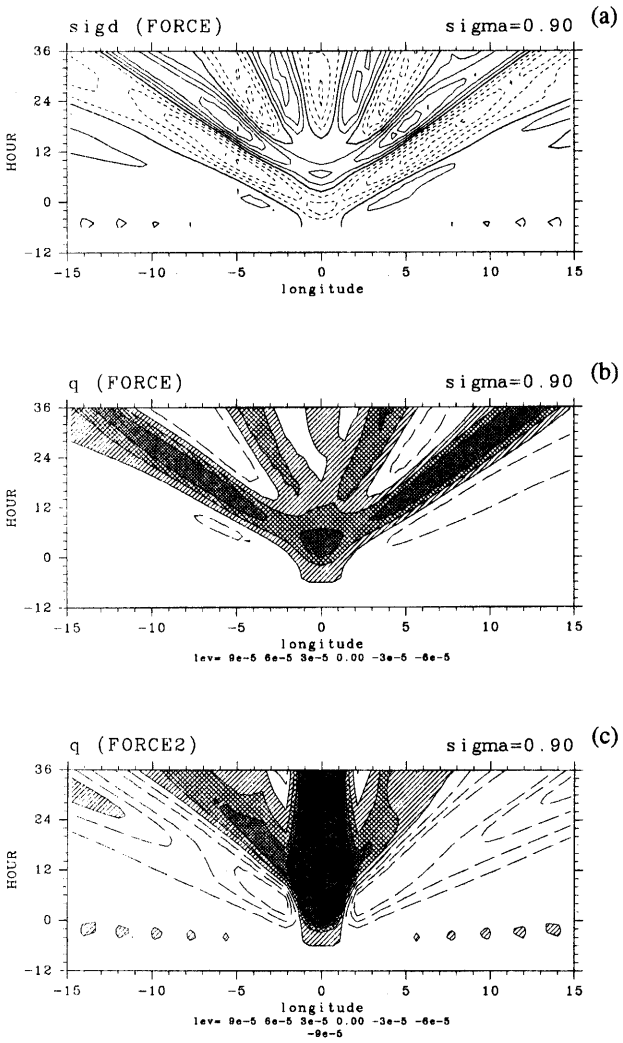

Fig. 12. Longitude-time sections of responses in the linear-response experiment. (a) sigma vertical velocity (positive downward) at $\sigma = 0.87$, (b) specific humidity at $\sigma = 0.90$, (c) specific humidity at $\sigma = 0.90$, but for modified bottom-heavy heating. Contour intervals is 2×10^{-5} s^{-1} for (a) and dashed contours indicates negative value. For (b) and (c), contour intervals is 3×10^{-5} and the deviation from the initial field is shown with the positive-value areas being shaded. Heavier shading indicates a larger value.

is considered that the differences in the results between LSC (Fig. 2b) and LOWLSC (Fig. 2c) are attributed to the difference in the profile of condensational heating.

In the top-heavy case, Fig. 12a, a downdraft appears in the heated region just after the heating decays. This downdraft seems to correspond to the downdraft in the full-model results. The emergence of the downdraft associated with a convective cloud is usually attributed to the cooling by the micro-

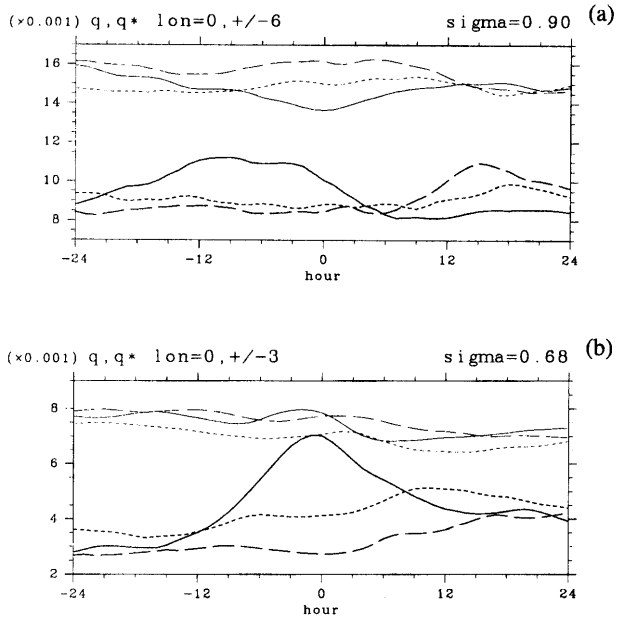

Fig. 13. Time sequence specific humidity q and saturated specific humidity q^* of the 'life cycle' composite for experiment LSC. Thick lines indicate specific humidity and thin lines indicate saturated specific humidity. (a) At $\sigma = 0.90$ level. Solid line: 0 degree longitude, dashed line: +6 degree longitude, dotted line: −6 degree longitude. (b) At $\sigma = 0.68$ level. Solid line: 0 degree longitude, dashed line: +3 degree longitude, dotted line: −3 degree longitude.

physical processes (evaporation, melting), or precipitation drag. In the present results, however, none of these effects are present and the downdraft is interpreted as a part of the dynamical behavior of gravity waves.

5.4 *Westward movement and eastward emergence of QPCC*

In order to further examine the development of cloud activity, especially its asymmetric behavior in the east-west direction, the development of specific humidity q and saturated specific humidity q^* (which is a function of temperature and pressure) is examined at different longitudes and levels and shown in Fig. 13. At 900 hPa level (Fig. 13a), the specific humidity q significantly increases around hour −15 at 0 degrees longitude (solid line), and around hour +12 at +6 degrees longitude (dashed line). These events occur just before the development of intense cloud activity (Fig. 7). Decreases in saturated specific humidity q^* due to cooling are seen almost simultaneously, but the amplitudes are smaller than those of the increases in specific humidity. Note that the relative humidity never reach 100 % because the composite technique averages both saturated and unsaturated cases. At the western point, −6 degrees longitude (dotted lines), the increase in q and the decrease in q^* both are too small to initiate strong cloud activity.

At 680 hPa level (Fig. 13b), a similar significant increase in q and a small decrease in q^* are seen just before the intense cloud activity: around hour −4 at 0 degrees longitude (solid line), and around hour +6 at −3 degrees longitude (dotted line). At the eastern point (+3 degrees – dashed line), however, the increase in q is smaller than at the western point. Moreover, compared between the eastern and western points, q is smaller and q^* is larger at the eastern point, and thus the relative humidity is much smaller, even before hour −12. These two differences, smaller existing relative humidity and a smaller increase in q, are considered to suppress the onset of cloud activity to the east.

The existing east-west contrast of relative humidity is consistent with the structure of SCC shown in Fig. 5b. This large-scale east-west contrast is due to the eastward movement of SCC, which will moisten and cool the troposphere. From another viewpoint, the moistness of the western region is attributed to the moistening and cooling effect of the eastward-propagating circulations associated with the QPCC of the previous generation: Fig. 13b indicates that the q and q^* at the eastern point around hour 12–24 reach almost the same level as those at the western point around hour −24––12.

For the asymmetry of the increase in q, an obvious candidate for the origin in this particular experiment (LSC) is the modeled beta effect. The asymmetry due to the modeled beta effect can be examined by the linear response described in the previous subsection. In the low-level ($\sigma = 0.90$) humidity field shown in Fig. 12a, the maximum humidity is a little higher to the east than to the west. In the upper level ($\sigma = 0.51$) shown in Fig. 14a, on the other hand, the maximum humidity is higher around −3 degrees west than around +3 degrees east. In this figure, the contours show the east-west antisymmetric part of the response, $(q(x) - q(-x))/2$, clearly indicating the larger moistening to the west than to the east. This is because the low-to-middle-level convergence (Fig. 14b), and thus the middle-level upward motion, is stronger to the west. As discussed in the Appendix, the east-west asymmetry of divergence due to the modeled beta effect develops linearly with time as,

$$\frac{D(x) - D(-x)}{2} \simeq -\frac{\beta t}{2}\frac{u(x) - u(-x)}{2}. \qquad (11)$$

Here $\bar{u} = (u(x) - u(-x))/2$ is the *symmetric* part of the response of zonal wind (see, (A17)), which approximately behaves as gravity waves in a non-rotating environment. This correspondence can be confirmed by comparing Fig. 14b and Fig. 14c. The beta effect acts on the low-to-middle-level zonal

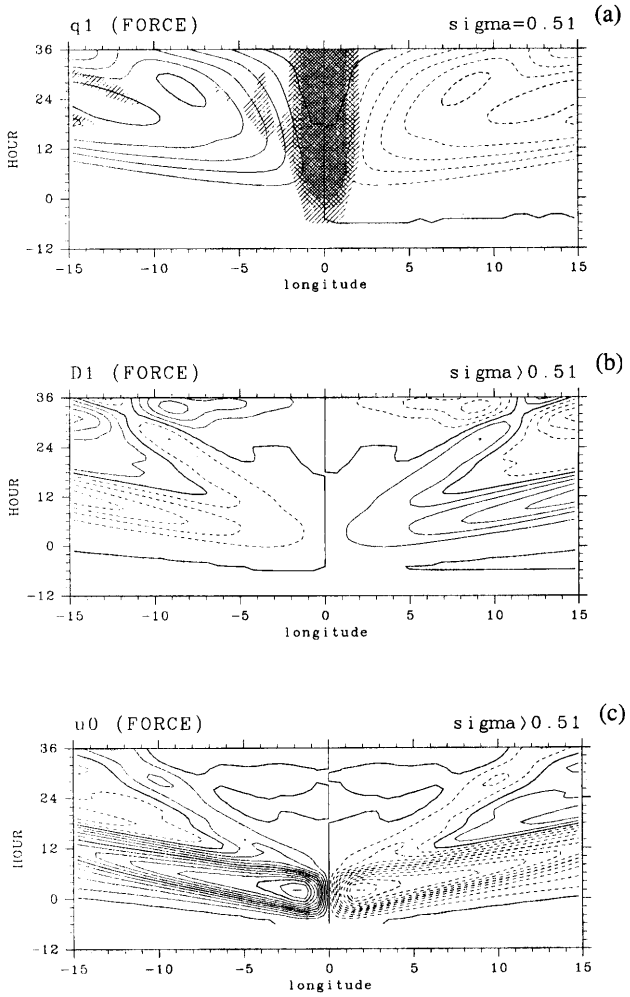

Fig. 14. Longitude-time sections of responses in the linear-response experiment. (a) Specific humidity at $\sigma = 0.51$ (positive deviations from initial are shown in shading) and its anti-symmetric part (contours). (b) anti-symmetric part of divergence integrated between $\sigma = 0.51$–1.0, (c) symmetric part of zonal wind integrated under $\sigma = 0.51$–1.0.

wind, which has opposite directions between the eastern and western regions, and anti-symmetrically modifies the divergence and upward motion. It is confirmed that these east-west asymmetric responses due to the modeled beta effect in the present two-dimensional model are not distorted artifacts of the 'shortwave approximation', but they are essentially similar to the responses in the three-dimensional model over a sphere (see, Appendix).

The westward-moving cloud cluster (QPCC) can be interpreted as a coupling between gravity wave and cloud activity. Because the cloud activity is mostly confined to the upper half of the troposphere, where the stratification is moist stable (Fig. 7), the coupled mode may not be unstable. Rather, it is considered a neutral coupled mode, in which condensational heating only partly cancels adiabatic cooling. The structure appearing in Fig. 4a, in which the temperature quickly drops at the time of a maximum updraft, seems consistent with this idea. The westward-moving cloud cluster (QPCC) will slowly decay owing to dissipation or other effects.

To the east of the original stationary cloud, although the shallow-mode low-level updraft occasionally forms weak low-level cloud activity, it cannot extend to a tall convective cloud. This is because the upward motion caused by this cloud activity is so weak and transient and the middle-level air is so dry that the mixture of the original dry middle-level air and advected moist low-level air is never saturated at the middle level. Convective cloud activity develops only after sufficient moistening and cooling have occurred both in the low and middle troposphere. This saturation initiates an explosive growth through CIFK and a development of QPCC of the next generation. To the west, on the other hand, an explosive growth of a convective cloud will not occur. This is because the stratification is already adjusted near neutral through westward-moving cloud activity (QPCC). Another reason is that the smaller increase in moisture to the west (Fig. 13a), which is considered partly due to the beta effect (Fig. 12b) and partly due to the downward motion excited by the top-heavy heating associated with westward-moving QPCC (Fig. 9a, Fig. 12a).

The possibility of the onset of the next convective cloud is considered highest when and where the humidity becomes largest. As discussed in the previous subsection (5.3; see also Fig. 11, Fig. 12a and 12b, and Fig. 13a and 13b), the largest upward displacement of low-level air and thus the largest humidity signal exists to the east just after the deep-mode updraft signal passes through, but before the shallow-mode updraft turns to a downdraft. Because the deep-mode updraft departs from the origin longitude later but with a faster speed than the shallow-mode updraft, these two updraft signals intersect, and the humidity becomes maximum around this intersection. It is about 15 hours ($\sim$ the period of the gravity waves) after the time of maximum heating and about 6 degrees ($\sim$ wavelength of the shallow mode) to the east of the original convective cloud. The quasi-periodic emergence of a new convective cloud (new QPCC) to the east of the original convective cloud (QPCC) causes the eastward movement of the SCC, which is the envelope of QPCC. However, we cannot discuss the horizontal scale of SCC and its propagation speed in detail because of the restricted sector geometry of the model and non-negligible error in the phase speed of the eastward gravity (Kelvin) wave of the scale of SCC due to the short-wave approximation (see, Appendix).

In experiment NOBETA (Fig. 2d), there exist not only SCCs similar to those in experiments MCA and LSC, but also westward-propagating SCCs with

eastward-propagating QPCCs. This indicates that the SCC-like structure, in which the larger-scale structure and the smaller-scale substructure move in opposite directions, can exist without the external origin of asymmetry. The mechanism can be understood by omitting the beta effect in the previous discussion. If the initial atmosphere is moister and colder to the west, the QPCC will move westward while the SCC will move eastward, and vice versa. The east-west contrast of relative humidity tends to be maintained by the QPCC-SCC life cycle, but the feedback is too weak to maintain the contrast persistently.

If there is some external origin of east-west asymmetry, one of the two modes of SCC (eastward moving and westward moving) can be selectively appeared. With the modeled beta effect, an eastward-moving SCC is selected because the asymmetry of the updraft helps the westward movement of QPCC. Similar selection of eastward-moving SCC is occurred in the experiments WISHE and SHEAR. In the experiment WISHE, the evaporation (not shown in figures) is generally large to the east of SCC because the easterly wind perturbations exists there on top of the mean easterly. This large evaporation will intensify the eastward-moving gravity-wave circulations associated with the SCC by the WISHE feedback. By incorporating mean wind shear (experiment SHEAR), the westward moving QPCC and eastward moving SCC can be selected in certain conditions due to dynamical asymmetry caused by the mean shear. The detailed mechanisms of the selection due to the effects of WISHE and mean shear are currently under research and will be discussed in separate papers. Moreover, the question which process (or some processes other than beta, WISHE, or shear) is most effective for the selection of the eastward moving SCC is beyond the scope of this paper. In order to answer the question, more detailed studies on sensitivities to the external parameters, preferably with three dimensional models without shortwave approximation, are required.

6. Summary and concluding remarks

The hierarchical structures of eastward-moving super cloud clusters (SCC) and embedded westward-moving cloud clusters with quasi-two-day periodicity (QPCC) are successfully simulated by a simple longitude-height two-dimensional model with simple moist processes. The simulated structures of both SCC and QPCC are found to be very similar to the observed structures described in Takayabu and Murakami (1991), and Takayabu et al. (1996).

The model results clearly show the life cycle of circulations and clouds and indicates the importance of interaction between gravity waves and clouds. The essence is schematically shown in Fig. 15. The cloud area starts as a low-level shallow cloud. Subsequently, the cloud grows deeper and deeper, to become deep cumulus convection, and then starts decaying from lower levels to higher levels. This convective cloud does not move horizontally during its growth. The growing process can be interpreted as due to CIFK (conditional instability of the first kind) triggered by low-level updraft and condensation. The decay is considered due to the advection of dry, low θ_e air from the ambient atmosphere. More than two vertical modes (deep-mode and shallow-mode — corresponds to so-called 'first baroclinic' and 'second baroclinic' mode in the troposphere) of gravity-wave packets are excited by the heating due to this cloud, propagating both eastward and westward. In the decaying stage, the upper-level cloud activity propagates westward, coupled with an updraft signal of gravity wave, and forms a westward-moving cloud cluster (QPCC). The QPCC in this stage is interpreted as a cloud activity coupled with a neutral wave. To the east, a deep convective cloud develops only after the low and middle levels are sufficiently moistened by the cooperation of updraft signals associated with shallow- and deep-mode updrafts. When a deep convective cloud develops to the east, it becomes the QPCC of the next generation. The quasi-periodic emergence of the new QPCC to the east causes the eastward movement of SCC, which is the envelope of QPCC. The life-cycle behavior of clouds and waves, especially a combination of stationary growing stage and propagation stage leads to slower eastward propagation of the whole system, compared from the propagation speed of shallow-mode gravity waves. The top-heavy heating profile is important to the excitation of shallow-mode gravity-wave cells and the subsequent generation of the new convective cloud to the east.

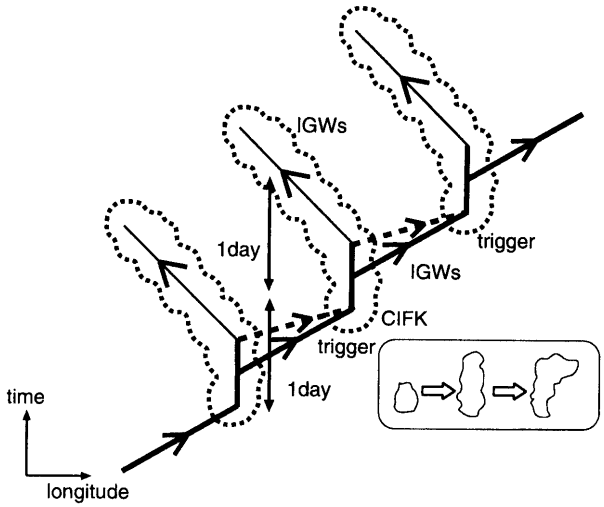

Fig. 15. Schematic representation of the processes involved in the SCC-QPCC development. A simplified version of Fig. 11.

The QPCC moves only westward because the

eastern region of the middle to upper troposphere is much drier than the western region. This east-west moisture contrast is the result of the existence of the QPCC of the previous generation to the west, which causes a moistening of the upper troposphere. Although both eastward- and westward-moving SCCs are possible, depending on the initial conditions, one of them (eastward-moving or westward-moving) will dominate if there is some external origin of east-west asymmetry. One of the candidates is the beta effect due to the rotation of the earth. It is shown that the modeled beta effect under 'shortwave approximation', which mimics the east-west asymmetry of the dynamics of gravity waves, helps the westward movement of QPCC and then the eastward movement of SCC. However, the conclusion on the possible importance of the beta effect is tentative, because the modeled beta effect by short-wave approximation captures only a part of many aspects of beta plane dynamics. This modeled beta effect simulates the east-west asymmetry of the wave behavior in qualitative and linear sense, but it may not correctly reproduce the qualitative behavior including the non-linear processes and meridional structures. Other candidates for asymmetry are the effect of basic wind shear and the WISHE feedback. Examination of relative importance of the external origins of the east-west asymmetry using three dimensional model are left as future works.

The fundamental time scale of the present mechanism of QPCC-SCC formation is the lifetime of the cloud in the stationary growth stage. This time scale, about half a day, is considered to be determined by the turn-over time of the convective circulation. This time-scale determines the period of excited gravity waves (about one day). Then the interval of formation of new convective clouds to the east, also about one day, is determined by the interplay of gravity waves of different vertical wavelengths (see, Fig. 15). The periodicity of two days, observing at a fixed longitude, can be explained by the combination of this one-day and the additional one-day for QPCC to travel westward. In our model, the turn-over time of the convection and lifetime of the cloud are considered determined by the grid size of the model. These timescales should be constrained by the timescale of smallest-scale gravity waves resolved in the model. In nature, however, the scales of the cloud cluster is considered to be determined by mesoscale dynamical and physical processes, which is not properly treated in the present model. Moreover, the diurnal cycle of insolation, which is neglected in this study, may also contribute the timescale of QPCC (Chen et al. 1996).

The present results show many characteristics in common with the results of Chao and Lin (1994, CL94). Thus, the mechanism proposed in the present study is considered very similar to the 'cloud-cluster teleinduction mechanism' proposed by CL94. However, it is found that the basic zonal wind, which CL94 considered essential, is not necessary for the breakdown of the east-west symmetry. On the other hand, the mechanism of SCC in Yano et al. (1995) is considered very different from that in the present study. The interaction between the gravity waves of different vertical wavelength, which is found to be essential to the present mechanism, cannot be represented by their shallow-water model. The eastward movement of cloud activity in their model is essentially due to the WISHE mechanism.

The result suggests that the fundamental origin of the disturbance energy of QPCC and SCC is CIFK. It is considered that CIFK works during the development of individual cumuli. The convective cloud activity in the model should be compared with groups of cumulus (mesoscale cloud system, MCS). Whether or not the CIFK concept is approximately valid for the development of the MCS is not obvious. However, the real MCS and the cloud activity in the present model seem to share many common characteristics, and some of them are considered important in the dynamics of the SCC and QPCC; a life-cycle behavior, a time scale of several hours to a day, and a top-heavy heating profile in the mature and decaying stages (Houze 1993). Thus the essential results of the present study may not be seriously distorted by the crude treatment of the cloud process.

In this paper, discussion is mainly focused on the results of experiment LSC, in which only the grid-resolvable process of condensation is considered. The results with the moist convective adjustment scheme (experiment MCA) appear qualitatively the same. The main difference is that the development of a convective cloud is faster and the appearance of QPCC is more regular and frequent in experiment MCA than in experiment LSC. This result seems reasonable because the MCA scheme will help the successive upward development through the complete vertical mixing within the unstable cloud layers. Except for this 'acceleration' of convective development, the MCA scheme shares similar characteristics with the LSC scheme – both schemes are activated only when and where grid-scale humidity exceeds a saturated value. For other types of schemes, for example those in which the convective onset is controlled mainly by low-level convergence (e.g., the scheme of Kuo 1974), the result might be totally different from the present results (cf., CL94; Numaguti and Hayashi 1991).

The present results indicate the importance of the interaction between gravity waves and clouds in the dynamics of the SCC. In particular, their transient, interactive, and life-cycle behaviors are essential. Such interaction may not only be applied to the dynamics of SCC, but it will also be involved in the dynamics of other tropical disturbances. Re-

cently, Hayashi and Golder (1994; 1997a,b) proposed the 'saturation-triggering mechanism' to explain the generation of large-scale tropical transient waves, such as Kelvin and mixed Rossby-gravity waves. They hypothesized that transient waves, coupled with moist convection, are triggered upon saturation by the intermittent onset of convective heat pulses. The present study suggests that the generation of the pulses and the subsequent development of convection in their mechanism can be interpreted as the interaction between gravity waves and clouds.

It will be a challenging future work to refine the gravity-wave dynamics examined in this study and to apply it to the phenomena other than SCC. Also left for future studies are more realistic simulation with finer resolution, including some important cloud physics, various effects of mean wind shear and WISHE, and an extension to a three-dimensional domain.

Acknowledgments

The main part of this work is done when the first author was a visiting research staff at Geophysical Fluid Dynamics Laboratory, under the Program in Atmospheric and Oceanic Sciences, Princeton University. The authors express special thanks to Dr. B.E. Mapes, for insightful discussions from the early stage of this work. We are grateful to Drs. S. Manabe and J.D. Mahlman for thoughtful comments and encouragement, and Drs. I.M. Held, and I. Orlanski for providing valuable comments. We also thank anonymous reviewers for providing useful comments for the improvement of this paper. Thanks are extended to Drs. Y.N. Takayabu, K. Sato, T.J. Dunkerton, J.D. Neelin, S.S. Chen, C.-D. Zhang, C.S. Bretherton, and R.A. Houze, Jr. for stimulating discussions. The GFD-DENNOU library is used for the drawings.

Appendix

Derivation of the shortwave approximation

For simplicity, the derivation of the shortwave approximation is discussed here based on the linear shallow water equations on the equatorial beta plane.

$$\frac{\partial u}{\partial t} = -\frac{\partial \phi}{\partial x} + \beta y v, \tag{A1}$$

$$\frac{\partial v}{\partial t} = -\frac{\partial \phi}{\partial y} - \beta y u, \tag{A2}$$

$$\frac{\partial \phi}{\partial t} = -C^2\left(\frac{\partial u}{\partial x} + \frac{\partial v}{\partial y}\right) + F. \tag{A3}$$

By differentiating (A1) by x and (A2) by y, respectively, and nondimentionalized with

$$(u,\ v,\ \phi,\ \partial/\partial x,\ \partial/\partial y,\ y,\ t)$$
$$= (U,\ V,\ CU,\ 1/L_x,\ 1/L_y,\ Y,\ L_x/C)$$

assuming that the primary balance is the same as that of the zonally-propagating gravity waves, these become,

$$\frac{\partial}{\partial t}\frac{\partial u}{\partial x} = -\frac{\partial^2 \phi}{\partial x^2} + \hat{\mu}\hat{\beta}\hat{\eta} y \frac{\partial v}{\partial x}, \tag{A4}$$

$$\hat{\mu}\hat{\gamma}\frac{\partial}{\partial t}\frac{\partial v}{\partial y} = -\hat{\gamma}\frac{\partial^2 \phi}{\partial y^2} - \hat{\beta} u - \hat{\beta}\hat{\eta} y \frac{\partial u}{\partial y}, \tag{A5}$$

$$\frac{\partial \phi}{\partial t} = -\frac{\partial u}{\partial x} - \hat{\mu}\hat{\gamma}\frac{\partial v}{\partial y} + F. \tag{A6}$$

where,

$$\hat{\beta} = \frac{\beta L_x^2}{C} = \left(\frac{L_x}{L_R}\right)^2,\ \hat{\gamma} = \left(\frac{L_x}{L_y}\right)^2,$$

$$\hat{\eta} = \frac{Y}{L_y},\ \hat{\mu} = \frac{V L_y}{U L_x}.$$

Here L_R is the equatorial radius of deformation: $L_R = \sqrt{C/\beta}$.

Assuming lowest meridional mode of the equatorial waves, it becomes $L_y \simeq L_R$ and then $\hat{\beta} = \hat{\gamma}$. From the balance of (A5). it should be $\hat{\mu} \leq 1$. If we define the nondimensional divergence D as,

$$D \equiv \frac{\partial u}{\partial x} + \hat{\mu}\hat{\beta}\frac{\partial v}{\partial y} \tag{A7}$$

(A4) +(A5) becomes,

$$\frac{\partial D}{\partial t} = -\frac{\partial^2 \phi}{\partial x^2} - \hat{\beta}\frac{\partial^2 \phi}{\partial y^2} - \hat{\beta} u + \hat{\beta}\hat{\eta} y \frac{\partial v}{\partial x} - \hat{\mu}\hat{\beta}\hat{\eta} y \frac{\partial u}{\partial y}. \tag{A8}$$

Now we assume that $\hat{\beta} \ll 1$ and $\hat{\eta} \ll 1$. The former condition assumes that the zonal scale of the disturbance is smaller than the equatorial radius of deformation, and the latter assumes that the equations are applied at the latitude sufficiently near the equator. By ignoring second-order ($O(\hat{\beta}\hat{\eta})$) terms,

$$\frac{\partial D}{\partial t} = -\frac{\partial^2 \phi}{\partial x^2} - \hat{\beta}\frac{\partial^2 \phi}{\partial y^2} - \hat{\beta} u \tag{A9}$$

From (A7)

$$u = \int D dx - \hat{\mu}\hat{\beta}\int \frac{\partial v}{\partial y} dx \equiv u^* - \hat{\mu}\hat{\beta} v^* \tag{A10}$$

where the integration constants are determined by the condition that the zonal mean of u, u^* and v^* should be zero. By replacing u in (A9) by (A10), and further ignoring second-order ($O(\hat{\beta}^2)$)terms,

$$\frac{\partial D}{\partial t} = -\frac{\partial^2 \phi}{\partial x^2} - \hat{\beta}\frac{\partial^2 \phi}{\partial y^2} - \hat{\beta} u^*. \tag{A11}$$

Finally, the term of $\partial^2\phi/\partial y^2$ is neglected due to lack of explicit y-dependence of the model. This term can be parameterized as $-\phi/L_R^2$ assuming the meridional structure of the equatorial waves. However, L_R depends on C and thus on the vertical scale of the motion, it is impossible to adequately apply this parameterization in multilevel models. Therefore, we neglect this term for simplicity. Then the dimensionalized equations become,

$$\frac{\partial D}{\partial t} = -\frac{\partial^2\phi}{\partial x^2} - \beta u^*, \tag{A12}$$

$$\frac{\partial \phi}{\partial t} = -C^2 D + F, \tag{A13}$$

$$\frac{\partial u^*}{\partial x} = D. \tag{A14}$$

The basic equation of the model (1)–(6) can be derived similarly by extending the procedure to the non-linear primitive equations. The divergence Eq. (1) should be written, more precisely, as

$$\frac{\partial D}{\partial t} + \frac{\partial}{\partial x}(u^* D) + \frac{\partial}{\partial x}\left(\dot{\sigma}\frac{\partial u^*}{\partial \sigma}\right) = -\beta u^* - \frac{\partial^2\phi}{\partial x^2} - \frac{\partial}{\partial x}\left(RT\frac{\partial \pi}{\partial x}\right). \tag{A15}$$

In this equation, some $O(\hat{\beta})$ terms in the non-linear advection terms are ignored. Then, in (1)–(6), u^* is replaced by u for simplicity. Note that this replacement is not an approximation but only a change of notation. The precise meaning of u in (1)–(6) is not the pure zonal wind, but it includes the contribution of the meridional wind.

Dispersion relation and east-west asymmetry under the shortwave approximation

Based on (A12)–(A14), the dispersion relation is calculated by assuming a sinusoidal perturbation as,

$$\omega = \pm\sqrt{k^2C^2 + \left(\frac{\beta}{2k}\right)^2} - \frac{\beta}{2k}, \tag{A16}$$

where ω is the frequency and k is the zonal wavenumber. The result for $C = 15$ m/s is shown in Fig. A1. It is seen that two solutions (dotted lines) given by (A16) reasonably reproduce the exact solutions of equatorial waves on a β plane (solid lines). The eastward propagating (positive frequency) wave behaves as the Kelvin wave, and the westward-propagating (negative frequency) wave behaves as the inertio-gravity wave of $n = 1$. However, in the low-wavenumber limit, the direction of the group velocity of the westward-propagating wave is wrong and the frequency of the eastward-propagating wave is too low.

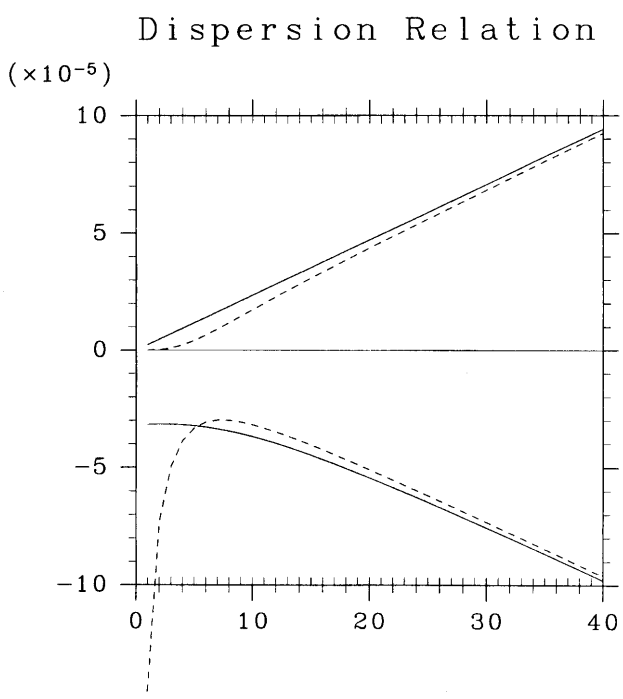

Fig. A1. Dispersion relations of a linear shallow-water version of the model for $c =$ 15 m/s. The abscissa is wavenumber ($k =$ 1 corresponds to 40,000 km wavelength) and the ordinate is frequency in 1/s. Dotted lines indicate the solution of dispersion relation (A16) and solid lines indicate the exact solution of equatorial waves on a beta plane (Matsuno 1966); Kelvin wave and $n = 1$ westward-propagating inertio-gravity wave.

In the followings, the east-west asymmetry of the solution of these equation is examined compared with that of the three dimensional equations. We define the 'symmetric part' (concerning longitude) as,

$$\begin{pmatrix}\bar{u}\\ \bar{\phi}\\ \bar{D}\end{pmatrix} = \frac{1}{2}\begin{pmatrix}u^*(x) - u^*(-x)\\ \phi(x) + \phi(-x)\\ D(x) + D(-x)\end{pmatrix}, \tag{A17}$$

and the 'anti-symmetric part' as,

$$\begin{pmatrix}u'\\ \phi'\\ D'\end{pmatrix} = \frac{1}{2}\begin{pmatrix}u^*(x) + u^*(-x)\\ \phi(x) - \phi(-x)\\ D(x) - D(-x)\end{pmatrix}. \tag{A18}$$

If the external forcing F as well as the initial condition is purely symmetric, the anti-symmetric part of response should come from the beta term. Then, $|u'|/|\bar{u}| \sim |\phi'|/|\bar{\phi}| \sim O(\hat{\beta})$. Ignoring terms of $O(\hat{\beta}^2)$, the equations for the symmetric part of (A12)–(A14) results in the equation of gravity waves in a non-rotational environment:

$$\frac{\partial^2\bar{D}}{\partial t^2} - C^2\frac{\partial^2\bar{D}}{\partial x^2} = \bar{F}, \tag{A19}$$

while the equations for the anti-symmetric part results in,

$$\frac{\partial^2 D'}{\partial t^2} - C^2 \frac{\partial^2 D'}{\partial x^2} = -\beta \frac{\partial \bar{u}}{\partial t}. \quad \text{(A20)}$$

The longitudinal asymmetry of the response in the presence of the beta effect is described by a forced response of (A20) with forcing of $-\beta\bar{u}$, which in turn is described by the equation of pure gravity wave (A19)

If the solution of (A19) is represented by

$$\bar{u} = \int u_k e^{ik(x-Ct)} dk,$$

the solution of (A20) with initial condition $D' = 0$ at $t = 0$ is

$$D' = -\frac{\beta t}{2} \int u_k t e^{ik(x-Ct)} dk = -\frac{\beta t}{2} \bar{u}. \quad \text{(A21)}$$

By extending this result to multi-level equations, we get,

$$\dot{\sigma}' \simeq \int_\sigma^1 D' d\sigma = -\frac{\beta t}{2} \int_\sigma^1 \bar{u} d\sigma. \quad \text{(A22)}$$

The corresponding equations on a three-dimensional equatorial β plane in the limit of $f \to 0$ are,

$$\frac{\partial^2 \bar{D}}{\partial t^2} - C^2 \left(\frac{\partial^2 \bar{D}}{\partial x^2} + \frac{\partial^2 \bar{D}}{\partial y^2} \right) = \bar{F}, \quad \text{(A23)}$$

and

$$\frac{\partial^2 D'}{\partial t^2} - C^2 \left(\frac{\partial^2 D'}{\partial x^2} + \frac{\partial^2 D'}{\partial y^2} \right) = -\beta \frac{\partial \bar{u}}{\partial t}. \quad \text{(A24)}$$

The Eqs. (A19) and (A20) are identical to the Eqs. (A23) and (A24) except for the difference of geometry. Then, the longitudinal asymmetry of the response is described in the two-dimensional system similar to that in the three-dimensional system, provided that the symmetric solution of (A19) is a good approximation of the solution of (A23). In the problem of heating response, this condition is considered to hold in the regions just to the west and to the east of the heating, where the inequality $\partial^2/\partial y^2 \ll \partial^2/\partial x^2$ is generally satisfied.

In order to further justify the representation of the beta effect in the two-dimensional model, three-dimensional calculations of a linear heating response are made. The heating is identical to (10) but with Gaussian latitudinal distribution centered at the equator. Figure A2 shows the result for the anti-symmetric part of divergence integrated between the $\sigma = 0.51 \sim 1.0$ levels. Comparing this with the two-dimensional result (Fig. 14b), it is considered that the two-dimensional model is capable of qualitatively reproducing the results of the three-dimensional model at least in a linear context.

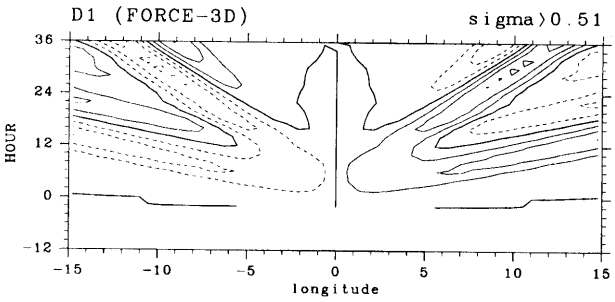

Fig. A2. Longitude-time section of response in the three-dimensional linear-response experiment. Anti-symmetric part of divergence integrated under $\sigma = 0.51$ is shown.

References

Bretherton, C.S., 1994: The nature of adjustment in cumulus cloud fields. *Representation of Cumulus Processes in Numerical Models*, 63–74. Meteorological Monograph, No. 46, Amer. Meteor. Soc.

——— and P.K. Smolarkiewicz, 1989: Gravity waves, compensating subsidence and detrainment around cumulus clouds. *J. Atmos. Sci.*, **46**, 740–759.

Chao, W.C. and S.-J. Lin, 1994: Tropical intraseasonal oscillation, super cloud clusters and cumulus convection schemes. *J. Atmos. Sci.*, **51**, 1282–1297.

Chen, S.S., R.A. Houze, Jr. and B.E. Mapes, 1996: Multiscale variability of deep convection in relation to large-scale circulation in TOGA COARE. *J. Atmos. Sci.*, **53**, 1380–1409.

Emanuel, K.A., 1987: An air-sea interaction model of intraseasonal oscillations in the tropics. *J. Atmos. Sci.*, **44**, 2324–2340

———, J.D. Neelin and C.S. Bretherton, 1995: On large-scale circulations in convective atmosphere. *Quart. J. Roy. Metetor. Soc.*, **120**, 1111–1143.

Gill, A.E., 1980: Some simple solutions for heat-induced tropical circulation. *Quart. J. Roy. Metetor. Soc.*, **106**, 447–462.

———, 1982: Studies of moisture effects in simple atmospheric models: the stable case. *Geophys. Astrophys. Fluid Dyn.*, **19**, 119–152.

Hayashi, Y., 1970: A theory of large-scale equatorial waves generated by condensation heat and accelerating the zonal wind. *J. Meteor. Soc. Japan*, **48**, 140–160.

——— and D. Golder, 1994: Kelvin and mixed Rossby-gravity waves appearing in the GFDL "SKYHI" general circulation model and the FGGE dataset: Implications for their generation mechanism and role in the QBO. *J. Meteor. Soc. Japan*, **72**, 901–935.

——— and ———, 1997a: United Mechanisms for the generation of low- and high-frequency tropical waves. Part I: Control experiments with moist convective adjustment. *J. Atmos. Sci.*, **54**, 1262–1276.

——— and ———, 1997b: United Mechanisms for the generation of low- and high-frequency tropical waves. Part II: Theoretical interpretations. *J. Meteor. Soc. Japan*, **75**, 775–797.

———, ——— and P.W. Jones, 1997: Tropical gravity waves and superclusters simulated by high-horizonlat-resolution SKYHI general circulation models. *J. Meteor. Soc. Japan*, **75**, 1125–1139.

Hayashi, Y.-Y. and A. Sumi, 1986: The 30–40 day oscillation simulated in an "aqua planet" model. *J. Meteor. Soc. Japan*, **64**, 451–467.

Houze, R.A., Jr., 1993: *Cloud Dynamics.* Academic Press, 570pp.

Itoh, H., 1989: The mechanism for the scale selection of tropical intraseasonal oscillations. Part I: Selection of wavenumber 1 and the three-scale structure. *J. Atmos. Sci.*, **46**, 1779–1798.

Kuo, H. L., 1974: Further studies of the parameterization of the influence of cumulus convection on large-scale flow. *J. Atmos. Sci.*, **31**, 1232–1240.

Lau, K.-M., T. Nakazawa and C.-H. Sui, 1991: Observations of cloud cluster hierarchies over the tropical western Pacific. *J. Geophys. Res.*, **96**, 3197–3208.

———, L. Peng, C.-H. Sui and T. Nakazawa, 1989: Dynamics of super cloud clusters, westerly wind burst, 30-60 day oscillation and ENSO: An unified view. *J. Meteor. Soc. Japan*, **67**, 205–219.

Lindzen, R.S., 1974: Wave-CISK in the tropics. *J. Atmos. Sci.*, **31**, 156–179.

Madden R.A. and P.R. Julian, 1994: Observations of the 40-50-day tropical oscillation – A review. *Mon. Wea. Rev.*, **122**, 814–837.

Manabe, S., J. Smagorinsky and R.F. Strickler, 1965: Simulated climatology of a general circulation model with a hydrologic cycle. *Mon. Wea. Rev.*, **93**, 769–798.

Mapes, B.E., 1993: Gregarious tropical convection. *J. Atmos. Sci.*, **50**, 2026–2037.

——— and R.A. Houze, Jr., 1993: Cloud clusters and super clusters over the oceanic warm pool. *Mon. Wea. Rev.*, **121**, 1398–1415.

Matsuno, T., 1966: Quasi-geostrophic motions in the equatorial area. *J. Meteor. Soc. Japan*, **44**, 25–43.

Nakazawa, T., 1988: Tropical super clusters within intraseasonal variations over the western Pacific. *J. Meteor. Soc. Japan*, **66**, 823–839.

Neelin, J.D., I.M. Held and K.H. Cook, 1987: Evaporation-wind feedback and low-frequency variability in the tropical atmosphere. *J. Atmos. Sci.*, **44**, 2341–2348.

Nicholls, M.E., R.A. Pielke and W.R. Cotton, 1991: Thermally forced gravity waves in an atmosphere at rest. *J. Atmos. Sci.*, **48**, 1869–1884.

Numaguti, A., 1993: Dynamics and energy balance of the Hadley circulation and the tropical precipitation zones: Significance of the distribution of evaporation. *J. Atmos. Sci.*, **50**, 1874–1887.

——— and Y.-Y. Hayashi, 1991: Behaviors of cumulus activity and the structures of circulations in an "aqua planet" model. Part I: The structure of the super clusters. *J. Meteor. Soc. Japan*, **69**, 541–561.

Sui C.-H. and K.-M. Lau, 1992: Multiscale phenomena in the tropical atmosphere over the western Pacific. *Mon. Wea. Rev.*, **120**, 407–430.

Takayabu, Y.N., 1994: Large-scale cloud disturbances associated with equatorial waves. Part II: Westward propagating inertio-gravity waves. *J. Meteor. Soc. Japan*, **72**, 451–465.

———, K.-M. Lau and C.-H. Sui, 1996: Observation of a quasi 2-day wave during TOGA COARE. *Mon. Wea. Rev.*, **124**, 1892–1913.

——— and M. Murakami, 1991: The structure of super cloud clusters observed in 1–20 June 1986 and their relationship to easterly waves. *J. Meteor. Soc. Japan*, **69**, 105–125.

Yano, J.-I., J.C. McWilliams, M.W. Moncrieff and K.A. Emanuel, 1995: Hierarchical tropical cloud systems in an analog shallow-water model. *J. Atmos. Sci.*, **52**, 1723–1742.

スーパークラウドクラスターの階層構造にかかわる重力波の力学

沼口 敦[1]
（東京大学気候システム研究センター）
林 良一
（プリンストン地球流体研究所）

東進する熱帯のスーパークラウドクラスター (SCC) と、その内部構造としての西進する準周期的なクラウドクラスター (QPCC) の階層構造を、簡単な湿潤過程を組み入れた経度高度断面の簡単な2次元モデルを用いて再現した。

モデルの結果は明確な雲活動のライフサイクルを示す。すわわち雲域は浅い下層の雲からはじまり、深い対流雲へと発達し、さらに加熱が上層に集中した後、衰退する。この雲の発達と衰退に応じて重力波の波束が励起され東西に伝播する。西に伝播する波は雲活動と結合して、西進するQPCCを形成する。一方東に伝播する波は直ちには深い雲活動とは結び付かない。下層および中層が十分湿りかつ冷却された後になってはじめて、深い対流雲が発達する。この東向き重力波の伝播による東側での新たな対流雲の準周期的な出現が、QPCCの包絡構造としてのSCCの東進をもたらす。

この階層構造の生成において、対流圏上層に加熱率の最大を持つような雲加熱の発達・減衰にともない、2つの鉛直モードの重力波が励起されることが本質的に重要であることが示される。特に浅い鉛直スケールの重力波セルにともなう上向きの気塊の変位が、新たなQPCCの出現において重要な役割を担っている。ただし、外部に起因する東西の非対称性要因が何も無いような状況では東進するSCCも西進するSCCも存在可能である。ベータ効果、平均東西風シアー、WISHE (風速依存エネルギー交換) 効果による蒸発の東西非対称などの要因によって東進するSCCが選択されうる。

1 現所属：北海道大学大学院地球環境科学研究科